Publicacions

originales

Rev. Esp. Med. Nuclear 18, 6 (442-445), 199

Determinación de la distancia focal y evaluación de la convergencia en colimadores de geometría focalizada

D PARETO ONGHENA[1], J PAVÍA SEGURA[2,4], I JUVELLS PRADES[3], C FALCÓN FALCÓN[3], D ROS PUIG[1,4]

[1]Laboratorio de Biofísica y Bioingeniería. Fac. Medicina. UB. [2]Servicio de Medicina Nuclear. Hospital Clínic. [3]Laboratorio de Óptica. Fac. Física. UB. [4]Institut d'Investigacions Biomèdiques August Pi i Sunyer (IDIBAPS).

Resumen.—*Objetivo:* Se presenta un método para el cálculo de parámetros intrínsecos en colimadores convencionales de geometría focalizada. El método permite determinar la distancia focal y evaluar la calidad en la convergencia del colimador a una línea focal única.

Material y métodos: Se adquieren imágenes de una fuente radiactiva colocada sucesivamente en una serie de puntos de coordenadas conocidas. Para el cálculo de la focal se desarrolla un método que minimiza la suma de distancias entre los puntos experimentales y las posiciones teóricas de detección de dichos puntos. La convergencia del colimador se evalúa mediante las intersecciones entre todos los pares de rectas que pasan por el punto fuente y su punto imagen experimental.

Resultados: Los resultados encontrados sobre dos colimadores muestran desviaciones del orden del 1,5% del valor de la focal real respecto a la focal nominal. Los resultados indican, asimismo, que los agujeros del colimador no convergen a una línea focal única sino a una zona focal, con desviaciones promedio respecto al foco real de σ_x = 2,5 mm y σ_z = 7,1 mm.

Conclusiones: Los errores respecto a los valores originales y la extensión de la zona focal permiten concluir que la calidad de los colimadores utilizados es aceptable.

PALABRAS CLAVE: SPECT. Colimador fan beam. Control de calidad.

DETERMINATION OF THE FOCUS AND ASSESSMENT OF THE FAN BEAM CONVERGENCE COLLIMATORS

Summary.—*Objective:* A method to calculate intrinsic parameters of fan beam collimators is presented. This method allows us to determine focal length and to assess the convergence of the collimator on a single focus line.

Material and methods: Images of a radioactive source located successively in a series of known coordinate positions are acquired. To determine the focal distance, a method has been developed that minimizes the sum of the distances between the experimental image point and the theoretical ones. Collimator convergence was evaluated by the intersections between all the pairs of lines drawn between the source location and its experimental image point.

Results: The results found between the two collimators showed that the actual focal length deviates 1.5% from the real focal value and the nominal focal length. The results also indicate that the collimator holes do not converge on a single focal line but rather on a focal area, with average deviations in regards to the real focus being σ_x = 2.5 mm and σ_z = 7.1 mm.

Conclusions: The errors in regards to the original values and the extension of the focal zone make it possible to conclude that the quality of the collimators used is acceptable.

KEY WORDS: SPECT. Fan beam collimator. Quality control.

Recibido: 15-7-99.
Aceptado: 12-8-99.

Correspondencia:
D Ros
Laboratori de Biofísica i Bioenginyeria
Facultat de Medicina, UB
Casanova, 143
08036 Barcelona
E-mail: domenec@medicina.ub.es

Rev. Esp. Med. Nuclear, 1999;18:442-445

INTRODUCCIÓN

Uno de los factores que determinan la calidad de la imagen en Medicina Nuclear es la limitación de la dosis que puede recibir el paciente. Como consecuencia de esta limitación los estudios presentan, en general, una baja relación señal/ruido debido a la escasa estadística de fotones. Por esta razón, el diseño de colimadores que permitan mejorar la detección ha constituido un área de trabajo de gran relevancia[1,2]. En este sentido, la utilización en SPECT de colimadores de geometría focalizada en lugar de colimadores paralelos permite mejorar la eficiencia y la resolución del sistema[3].

Los parámetros intrínsecos del colimador tienen una incidencia directa sobre la calidad de las imágenes obtenidas por lo que es importante realizar un riguroso control de calidad para ajustar los valores. En particular, la distancia focal es un parámetro que debe ser determinado con precisión, ya que la reconstrucción de un estudio con una focal distinta de la real

puede generar artefactos que dificulten la cuantificación posterior[4].

En la literatura aparecen diversos métodos para el cálculo de la focal[5-7]. Para aplicar estos métodos es necesario conocer previamente el valor real de los parámetros que intervienen en el cálculo. La utilización de los parámetros nominales puede conducir a errores significativos en la determinación de la distancia focal.

El objetivo de este trabajo es desarrollar un método autoconsistente para el cálculo de la focal real, que permita caracterizar el colimador y evaluar su convergencia al foco sin el conocimiento previo de alguno de los parámetros.

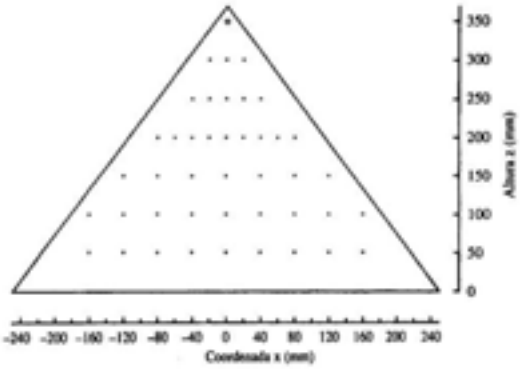

FIG. 1.—*Esquema de la disposición de los orificios en el soporte de metacrilato construido para conocer con precisión la posición de la fuente.*

MATERIAL Y MÉTODOS

Se ha evaluado la convergencia de dos colimadores *fan beam* de alta resolución (Van Mullekom, Holanda) de una gammacámara de doble cabezal Helix (Elscint, Haifa). Ambos colimadores tienen campo rectangular de 530 × 250 mm², agujeros hexagonales de longitud L = 40 mm, focal nominal F = 350 mm y distancia entre el plano de detección y la parte posterior del colimador B = 8 mm.

El método propuesto consiste en determinar las coordenadas del punto focal que minimizan la suma de distancias entre los puntos experimentales y teóricos de las imágenes de una fuente radiactiva colocada sucesivamente en puntos de coordenadas conocidas.

Obtención de las imágenes de la fuente

Como fuente se ha utilizado un capilar de 60 mm de longitud y 1,56 mm de diámetro que se ha llenado de ^{99m}Tc con una actividad de 25 MBq. Para controlar con precisión las coordenadas de la fuente se construyó un soporte de metacrilato, con 42 orificios para colocar el capilar. La figura 1 muestra un esquema, realizado a escala, con las posiciones de los orificios que están a 5, 10, 15, 20, 25 y 30 cm de altura respecto al plano del colimador. La máxima separación angular de la perpendicular que pasa por el centro del colimador es de 28°. No se consideraron posiciones de la fuente en ángulos superiores para evitar que la imagen quedara fuera del campo de detección. La colocación del soporte sobre la gammacámara se muestra en la figura 2. Para cada una de las posiciones de la fuente se adquirió una imagen de 256 × 256 píxels utilizando 2 bytes por píxel. El tamaño nominal del píxel fue de 2,21 mm y el tiempo de adquisición de 60s.

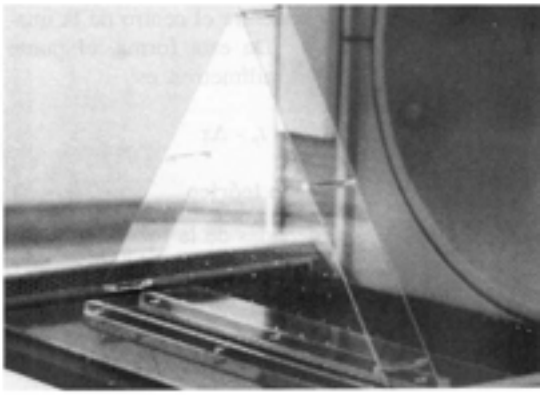

FIG. 2.—*Soporte de metacrilado colocado directamente sobre el colimador de uno de los cabezales de la gammacámara.*

Cálculo del punto imagen experimental

La figura 3 muestra esquemáticamente el foco (x_f, z_f), la posición de la fuente (x_0, z_0), la línea que los une y su intersección con el plano de detección que es el punto imagen teórico [x_t, - (L + B)]. Próximo a él se encontrará el punto imagen experimental [x_e, -(L + B)].

Para cada una de las imágenes, el perfil de actividad en la dirección horizontal representa la LSF *(Line Spread Function)* de la fuente. La LSF se ajustó por mínimos cuadros a una gaussiana[8], tomando el centro de la gaussiana, m, como la posición de detección.

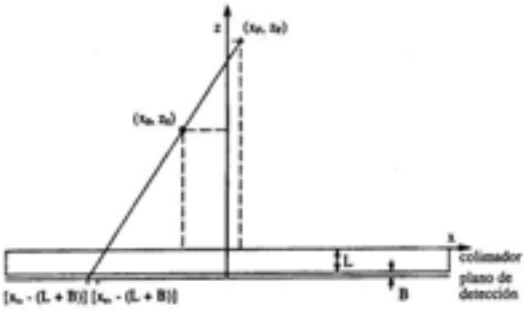

FIG. 3.—*Esquema de los elementos utilizados en el método de minimización.*

Para hallar el punto imagen experimental hay que multiplicar este valor por el tamaño del píxel t_p y restar el posible desplazamiento Δx que pueda haber debido a la no coincidencia entre el centro de la imagen y el del colimador. De esta forma, el punto imagen experimental, en milímetros, es:

$$x_e = m \cdot t_p - \Delta x$$

Cálculo del punto imagen teórico

Conocidas las coordenadas de la fuente (x_0, z_0) y tomando unas coordenadas generales del foco (x_F, z_F), se construye la recta que pasa por ambos puntos:

$$z - z_F = \frac{(z_0 - z_F) \cdot (x - x_F)}{(x_0 - x_F)}$$

Prolongado el rayo hasta $z = -(L + B)$ se obtiene el punto imagen teórico, en milímetros, x_t:

$$x_t = x_F - \frac{(L + B + z_F) \cdot (x_0 - x_F)}{(z_0 - z_F)}$$

Minimización de los errores y cálculo de la focal

Una vez obtenidos los puntos imagen teórico y experimental, se define la función de mérito a minimizar:

$$\text{RMS} = \frac{\sqrt{\sum_{i=1}^{N} (x_{ti} - x_{ei})^2}}{N} = \frac{\sqrt{\sum_{i=1}^{N} [x_{ti} - (m_i \cdot t_p - \Delta x)]^2}}{N}$$

donde el sumatorio se extiende sobre las N medidas realizadas.

Para la minimización se utilizó el algoritmo *Simplex*[9] con la implementación descrita por Press[10]. Como resultado se obtuvo el ajuste conjunto de las coordenadas del foco (x_F, z_F) y los parámetros t_p y Δx. El parámetro t_p se incluyó como una variable en la rutina de minimización para comprobar la posible divergencia entre el valor nominal y el real. El algoritmo parte de unas estimas iniciales de los cuatro parámetros, cuyo valor va cambiando hasta encontrar los que minimizan la función de mérito.

Evaluación de la convergencia del colimador

Concluido el ajuste del foco, se estudió la convergencia del colimador calculando las intersecciones entre todos los pares de rectas que pasan por el punto en el que está situada la fuente y su correspondiente punto imagen experimental. Las rectas que formaban un ángulo menor de 5° se excluyeron ya que pequeños errores en la localización del punto imagen experimental o la fuente pueden conducir a una gran incertidumbre en el punto de intersección. La representación de todas las intersecciones en un diagrama bidimensional permite evaluar la calidad del colimador en referencia a la convergencia a un foco único.

RESULTADOS

En la tabla I se muestran los valores iniciales y los obtenidos tras el proceso de minimización para las coordenadas del foco (x_F, z_F), el tamaño del píxel t_p, y el desplazamiento entre centros Δx, para cada cabezal. Los valores t_p y Δx ajustados fueron utilizados en el cálculo de las intersecciones entre todos los pares de rectas que pasan por el punto fuente y su correspondiente punto imagen experimental. La representación del histograma bidimensional de los puntos de intersección se muestra en forma de imagen en la figura 4. La imagen, que permite evaluar la conver-

Tabla I
PARÁMETROS INICIALES Y FINALES TRAS EL AJUSTE PARA CADA CABEZAL (en mm)

	x_F	z_F	t_p	Δx
Inicial	0,0	350,0	2,21	0,0
Cabezal 1	0,5	355,5	2,22	-1,6
Cabezal 2	0,0	355,0	2,22	0,5

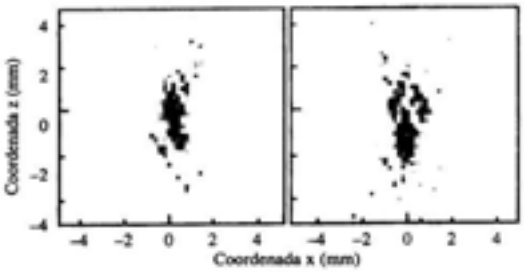

FIG. 4.—*Histograma bidimensional de los puntos de intersección entre todos los pares de rectas construidas a partir del punto imagen experimental y el punto que localiza la fuente en el plano, para el cabezal 1 (izquierda) y el 2 (derecha).*

gencia del colimador, se representa en escala de grises correspondiendo la máxima frecuencia a 7 intersecciones para el cabezal 1 y a 6 intersecciones para el cabezal 2. La amplitud del intervalo utilizado en ambos ejes fue de 0,5 mm.

DISCUSIÓN

La distancia z_F no coincide con la nominal, observándose diferencias de 5 mm que representan un error del 1,53% para el cabezal 1 y del 1,43% para el cabezal 2. Respecto al tamaño de píxel, las divergencias son menores del 1% por lo que resultan poco destacables.

En la figura 4 se puede observar para cada colimador el alejamiento del comportamiento ideal ya que la imagen no es un punto. Resulta entonces más conveniente hablar de una zona focal en lugar de un foco único. Las diferencias entre las dos imágenes es debida a las diferencias intrínsecas entre los dos colimadores.

Las desviaciones respecto al foco obtenido tras la minimización son $\sigma_x = 2{,}2$ mm y $\sigma_z = 6{,}3$ mm para el cabezal 1, $\sigma_x = 2{,}8$ mm y $\sigma_z = 7{,}9$ mm para el cabezal 2. Los valores de σ_x y σ_z pueden ser tomados como índices cuantitativos que reflejan la calidad de focalización del colimador.

El cálculo del promedio de las desviaciones, en valor absoluto, entre el punto imagen teórico y el experimental de la fuente, antes y después del proceso de minimización es un parámetro que refleja la calidad y mejora obtenida con el método propuesto. Tomando los parámetros iniciales, esta desviación promedio era de 3,5 mm para del cabezal 1 y de 3,0 mm para el cabezal 2; con los parámetros ajustados las desviaciones pasan a ser de 1,9 mm y 1,1 mm respectivamente.

Como objeto de estudio para un posterior trabajo queda analizar el efecto de estas desviaciones sobre la calidad de la imagen reconstruida a pesar que, los errores respecto los valores originales y la extensión de la zona focal, permiten concluir que la calidad de los colimadores utilizados es aceptable.

AGRADECIMIENTOS

Este trabajo ha sido financiado en parte por la CICYT (SAF96/0062, SAF99/0137).

BIBLIOGRAFÍA

1. Tsui BMW, Gullberg GT, Edgerton ER, Gilland DR, Perry JR, McCartney WH. Design and clinical utility of a beam collimator for SPECT imaging of the head. J Nuc Med 1986;27:810-9.
2. Moore SC, Kouris K, Cullum I. Collimator design for single photon emission tomography. Eur j Nuc Med 1993;19:138-50.
3. Jaszczak RJ, Chang LT, Murphy PH. Single photon emission computed tomography using multi-slice fan beam collimators. IEEE Trans Nucl Sci 1979;26:610-8.
4. Loncaric S, Chang W, Huang G, Liu J. Assessing the quality of focussing for fan beam collimators. J Nuc Med 1995;36: 109p.
5. Liu J, Loncaric S, Huang G, Chang W. The focussing quality of commercial fan beam collimators. J Nucl Med 1996;27:207p.
6. Formiconi AR. Geometrical response of multihole collimators. Phys Med Biol 1998;43:3359-79.
7. Mahowald JL, Robins PD, O'Connor MK. The evaluation and calibration of fan beam collimators. Eur J Nuc Med 1999;26:314-9.
8. Frey EC, Tsui BMW, Gullberg GT. Improved estimation of the detector response for converging beam collimators. Phys Med Biol 1998;43:941-50.
9. Nelder JA, Mead R. A simplex method for function minimazation. Comput J 1996;7:308-13.
10. Press WH, Teulosky SA, Vetterling WT, Flannery BP. Numerical Recipes in C (second edition). Cambridge University Press 1992.

Original article

Characterisation of fan-beam collimators

Deborah Pareto[1, 2], Javier Pavía[2, 3], Carles Falcón[1], Ignacio Juvells[4], Albert Cot[5], Domènec Ros[1, 3]

[1] Laboratori de Biofísica i Bioenginyeria. Facultat de Medicina. Universitat de Barcelona, Casanova 143, 08036 Barcelona, Spain
[2] Servei de Medicina Nuclear, Hospital Clínic, Barcelona, Spain
[3] Institut d'Investigacions Biomèdiques August Pi i Sunyer (IDIBAPS), Barcelona, Spain
[4] Departament de Física Aplicada i Òptica, Facultat de Física. Universitat de Barcelona, Barcelona, Spain
[5] Departament de Física i Enginyeria Nuclear, Universitat Politècnica de Catalunya, Barcelona, Spain

Received 15 July and in revised form 16 October 2000 / Published online: 22 December 2000
© Springer-Verlag 2000

Abstract. Fan-beam collimators offer a good balance between resolution and noise. The collimator response may be included in iterative reconstruction algorithms in order to improve single-photon emission tomography (SPET) resolution. To this end, accurate determination of the focal region and characterisation of the collimator response as a function of the source co-ordinates must be performed. In this paper, a method to characterise fanbeam collimators is evaluated. First, we calculated the real focal region and the accuracy of the collimator convergence. Then, we confirmed the hypothesis that Gaussian distributions adequately fit the collimator responses, although no individualised treatment was performed for the tails of detector response which are associated with scattering and septal penetration. Finally, analytical functions were used to model the resolution and sensitivity. The parameter values in these functions were obtained from experimental measures by non-linear regression fitting. Our findings show differences of 1.43% between nominal and real focal length and standard deviations of 2.5 mm in the *x*-direction and 7.1 mm in the *y*-direction for the focal convergence. The correlation coefficients between experimental and predicted values were 0.994 for resolution and 0.991 for sensitivity. As a consequence, the proposed method can be used to characterise the collimator response.

Keywords: Single-photon emission tomography – Collimators – Fan-beam collimators – Quality control

Eur J Nucl Med (2001) 28:144–149
DOI 10.1007/s002590000436

Domènec Ros (✉)
Laboratori de Biofísica i Bioenginyeria, Facultat de Medicina,
Universitat de Barcelona, Casanova 143, 08036 Barcelona, Spain
e-mail: domenec@medicina.ub.es
Tel.: +34-93-4024515, Fax: +34-93-4024516

Introduction

Considerable progress has been made in tomographic reconstruction in single-photon emission tomography (SPET) as a result of technological advances. On the one hand, the recent inclusion of transmission imaging systems in SPET gamma cameras has enabled us to obtain attenuation maps simultaneously with emission images. On the other hand, the increasing power of computers as well as the introduction of the ordered subsets-expectation maximisation algorithm (OS-EM) [1] has allowed us to reconstruct images within an acceptable time. Thus, it is possible to understand the growing interest in iterative reconstruction algorithms that has been witnessed during recent years. These algorithms may model the projection process and allow us to correct attenuation and spatially variant collimator response in the reconstruction process.

Sensitivity and resolution should be modelled as a function of the source co-ordinates in order to include the spatially variant detector response in the transition matrix. Our group has previously worked in iterative reconstruction algorithms [2, 3] and has achieved a modelling for parallel collimators. In agreement with other authors, a linear function of the full-width at half-maximum (FWHM) with respect to the source-collimator distance was found. This characterisation, which is easy for parallel collimators, becomes more difficult for fan-beam collimators. The FWHM and sensitivity in these collimators depend on the lateral position of the source and the source-collimator distance. Formulations for the spatial resolution and sensitivity have already been obtained [4, 5, 6, 7, 8]. Final expressions do not always coincide because different hypotheses have been introduced into the formulation.

In this paper a method to characterise a fan-beam collimator is proposed. To establish a model which is as realistic as possible, it is important to have performed previously an evaluation of the collimator parameters [9]. For this reason, determination of the real focal region is

included. The method allows us to assess the accuracy of the convergence of the hole directions to the focal line and to determine both the spatial resolution and the sensitivity as a function of source co-ordinates. Our approach is based on experimental measurements. Thus, not only is the geometric response considered but also septal penetration, collimator scatter and the detector response.

Materials and methods

Experimental line spread function (LSF). Experimental measures were carried out in a Helix dual-headed gamma camera (Elscint, Haifa) using cast fan-beam collimators (Van Mullekom, Holland). Both collimators had a rectangular field of view (FOV) of 530×250 mm, a nominal focal length F=350 mm, side of hexagonal hole w=0.866 mm, length L=40 mm and centre-to-centre hole distance σ_s=1.7 mm. We assumed that the distance between the back collimator face and the detector plane was B=8 mm. The line source was a capillary filled with 25 MBq of technetium-99m solution. The capillary was 70 mm in length (60 mm filled with the ^{99m}Tc solution) with an internal diameter of 1.1 mm.

To minimise the source location error, a support was constructed from Lucite (Ineos Acrylics Inc.). The support was constituted by two triangle sheets separated by 60 mm. Each sheet had a thickness of 2 mm, a base of 500 mm and a height of 360 mm. Forty-two holes were bored into the two support sheets into which the capillary was introduced. The holes were arranged in six rows located at 50, 100, 150, 200, 250 and 300 mm from the collimator face (Fig. 1). The maximum angle with respect to the central axis was 32° so that the source image did not fall outside the detection field. The acquisition matrix was 256×256 pixels, with a pixel width of 2.21 mm, two bytes per pixel and an acquisition time of 60 s.

Focal region. The experimental device was also used to characterise the focal region. In order to obtain values which quantitatively characterise the focal region, the actual focal length and the accuracy of the collimator convergence were obtained. The actual focal length was measured as the perpendicular distance from the focal line to the collimator front plane. For this purpose we followed the methodology described in an earlier work [10]. The method is

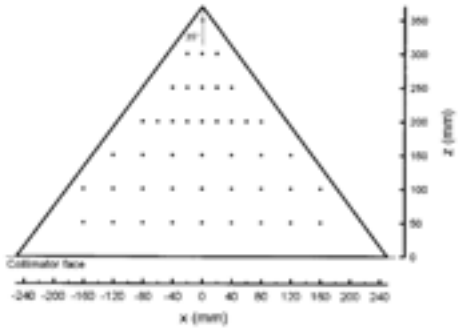

Fig. 1. Scheme of the experimental set up showing the hole distribution

based on determining the focal length which minimises the residuals between theoretical, x_{ti}, and experimental, x_{ei}, impacts of the 42 source points on the detection plane:

$$\mathrm{RMS} = \frac{\sqrt{\sum_{i=1}^{N}\left(x_{ti} - x_{ei}\right)^2}}{N}$$

x_{ti} is obtained from the intersection of the straight line passing through the source point (x_{0i}, z_{0i}) and the focal point (x_F, z_F) with the detector plane, $z = -(L+B)$:

$$x_{ti} = x_F - \frac{(L + B + z_F)\cdot\left(x_{0i} - x_F\right)}{\left(z_{0i} - z_F\right)}$$

and x_{ei} is calculated as:

$$x_{ei} = m_i \cdot t_p - \Delta x$$

where m_i is the centre, in pixels, of a Gaussian distribution fitted to the LSF, t_p is the pixel width and Δx takes into account the hypothetical shift between the geometric and electronic detector centres. Fitting was carried out by using the Simplex downhill algorithm [11] with the implementation described in [12].

The collimator convergence was assessed by calculating and plotting the intersect points between the pairs of straight lines passing through the source points and their corresponding experimental impact on the detector plane. Lines forming angles less than 5° were excluded to avoid high errors at the intersection points. These points were plotted in a x-z bidimensional diagram and the standard deviations in the x- and z-directions were calculated in order to quantitatively characterise the accuracy of the collimator convergence.

Intrinsic resolution. Intrinsic resolution was calculated by using a collimated source and removing the fan-beam collimator. The source consisted of a small cylinder which had a diameter of 2 mm and a height of 3 mm and was filled with 15 MBq of ^{99m}Tc solution. For collimation, the source was placed at the bottom of a solid block of lead 30 mm in height with a cylindrical cavity with a diameter of 1 mm. A Gaussian distribution was fitted to the experimental data and the standard deviation was calculated.

Spatial resolution. We assumed that the LSF is well characterised by a Gaussian distribution [13] and, as a consequence, the spatial resolution was measured as the standard deviation of the LSF. To assess the goodness of this assumption, the third (bias) and fourth (kurtosis) order mean moments of the distribution were calculated. These statistical parameters reflect the degree of difference with respect to a normal distribution.

In order to model the detector response, the standard deviation function $\sigma=\sigma(z_0, \theta)$ should be explicitly obtained. In the expression, z_0 represents the vertical distance from the point source to the front face of the collimator and θ is the angle between the normal and the straight line passing through the source point and the focal line. The value of σ depends on both the geometric contribution of the collimator, σ_c, and the intrinsic resolution, σ_i, of the detector. As far as the geometric contribution is concerned, if the intensity distribution is triangular, then FWHM=x_M, where x_M is the maximum distance reached by photons emitted in z_0 over the detector plane. We assume that for an intensity distribution different from the triangular one, the FWHM is proportional to x_M, FWHM=$k_1 \cdot x_M$, and, as a consequence, if a Gaussian distribution is considered, σ_c=FWHM/2.3548=0.4246·$k_1 \cdot x_M$=$a \cdot x_M$. To determine x_M, we impose that the ray from the source point $P(z_0, 0)$

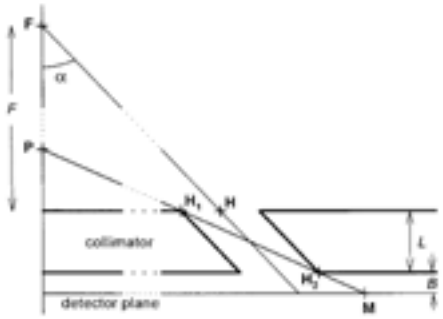

Fig. 2. Scheme showing the maximum distance x_M reached on the detector plane by the photons emitted from the source point P. The co-ordinates of the points in figure are: $\mathbf{F}(0,F)$, $\mathbf{P}(0,z_0)$, $\mathbf{H}(x_M, 0)$, $\mathbf{H_1}\left(x_H-\frac{w}{\cos\alpha},0\right)$, $\mathbf{H_2}\left(\frac{F+L}{F}x_H+\frac{w}{\cos\alpha},-L\right)$, $\mathbf{M}(x_M, -L-B)$

to the point $M(x_M, -L-B)$ passes through the front anterior limit of the hole $H_1\left(x_H-\frac{w}{\cos\alpha},0\right)$ and the back posterior H_2 $\left(\frac{F+L}{F}x_H+\frac{w}{\cos\alpha},-L\right)$ (Fig. 2). The centre of the hole is $H(x_M, 0)$. Thus, x_M is obtained as a function of the source point co-ordinates:

$$x_M = \pm\frac{w\cdot F\cdot(2z_0+L)}{\sqrt{L^2\cdot(F-z_0)^2-w^2\cdot(2z_0+L)^2}}$$

and taking into account that:

$$x_M=\frac{(z_0+L+B)}{z_0}x_{H_1}=\frac{(z_0+L+B)}{z_0}(x_H-w/\cos\alpha)$$

then:

$$x_M=\frac{w\cdot(z_0+L+B)\cdot(2F+L)}{\sqrt{L^2\cdot(F-z_0)^2-w^2\cdot(2z_0+L)^2}}$$

and, as a consequence:

$$\sigma_i(z_0,0)=\frac{a\cdot w\cdot(z_0+L+B)\cdot(2F+L)}{\sqrt{L^2\cdot(F-z_0)^2-w^2\cdot(L+2z_0)^2}}$$

where a is the constant to be determined. For displaced source positions of the z-axis, $P(z_0,\theta)$, we assume:

$$\sigma_i(z_0,\theta)=\frac{a\cdot(z_0+L+B)\cdot(2F+L)}{\sqrt{L^2\cdot(F-z_0)^2-w^2\cdot(L+2z_0)^2}}\cdot\frac{1}{\cos\theta}$$

It can be observed that when $F\to\infty$, the well-known linear dependence of σ with z_0 is obtained:

$$\lim_{F\to\infty}\sigma(z_0)=\frac{2\cdot a\cdot w\cdot(z_0+L+B)}{L}$$

To include the detector response we assumed that the intrinsic resolution was Gaussian. The convolution with the geometric collimator response was then performed. Since the convolution of two Gaussian distributions is also a Gaussian distribution, with $\sigma=\sqrt{\sigma_i^2+\sigma_r^2}$, the total spatial resolution was then obtained as:

$$\sigma(z_0,\theta)=\sqrt{\sigma_i^2+\sigma_r^2(z_0,\theta)}$$
$$=\sqrt{\sigma_i^2+\left(\frac{a\cdot w\cdot(z_0+L+B)\cdot(2F+L)}{\sqrt{L^2\cdot(F-z_0)^2-w^2\cdot(L+2z_0)^2}}\frac{1}{\cos\theta}\right)^2} \quad (1)$$

Non-linear regression was used to fit function (1) to the experimental σ values and determine the value of a. Fitting was carried out by using the Simplex downhill algorithm.

Sensitivity. The experimental sensitivity for each of the 42 source locations was obtained as the integral of the LSF profile [13]. An average over ten central rows was carried out in order to obtain more accurate results.

To characterise the collimator response, dependence of the sensitivity on source co-ordinates $s=s(z_0, \theta)$, should also be obtained. This function is a product of two terms. The first term is a constant related to intrinsic collimator parameters and the second term reflects the angular dependence. Following the geometrical arguments proposed in the literature [4, 7, 8], the sensitivity can be stated as:

$$s(z_0,\theta)=k\frac{(F+L)}{(F-z_0)}\cos^n\theta \quad (2)$$

Two angular dependencies have been proposed in earlier works, n=2 [6] and n=1 [8]. The fitting of function (2) to experimental sensitivity values will enable us to determine the best values for k and n. Fitting was carried out by means of the Simplex downhill algorithm.

Results and discussion

Experimental LSF

Gaussian distributions were fitted to the experimental LSFs. Figures 3 and 4 show the experimental LSF (dots) and the fitted curve (solid line) for two different z co-ordinates of the source. In these figures, the source position is represented as $P(z,\theta)$, where z is the source-to-collimator perpendicular distance (in mm), and θ is the aperture source angle (in degrees). The results for the source located in (150,0) and (150,–30.3) are shown in Fig. 3. The coefficients of determination of the fitting were r^2=0.999 and r^2=0.998, respectively. When the source was located in (300,0) and (300,–19.8), the coefficients were r^2=0.998 and r^2=0.996 (Fig. 4). The mean and standard deviation of r^2 for the 42 fittings was 0.999±0.001 for head 1 and 0.998±0.003 for head 2.

To calculate the third and fourth moments we used the interval $[m-3\sigma, m+3\sigma]$ where m is the x co-ordinate of the fitted Gaussian distribution and σ the standard deviation. Thus, after fitting and determining m and σ, the raw data (once corrected by background and decay) were used to calculate the moments. Comparison of the third and fourth moments of the experimental LSFs for θ=0° and for the maximum aperture angle was not statistically significant. These results, the high values of the coefficients of determination described above and the plots in Figs. 3 and 4 indicate that a Gaussian distribution accurately fits the experimental LSFs.

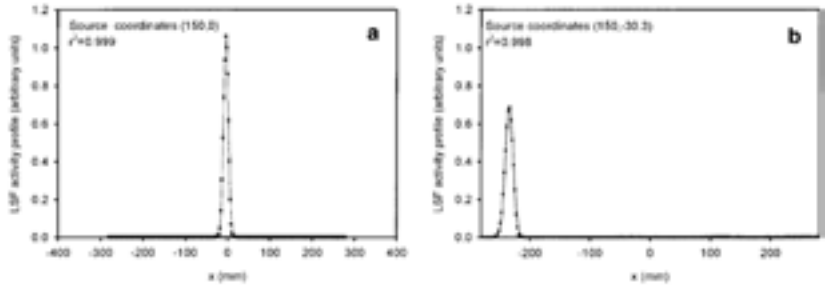

Fig. 3. Experimental (*dots*) and fitted (*solid line*) activity profiles of the LSFs at z=150 mm for θ=0° (**a**) and θ=−30.3° (**b**)

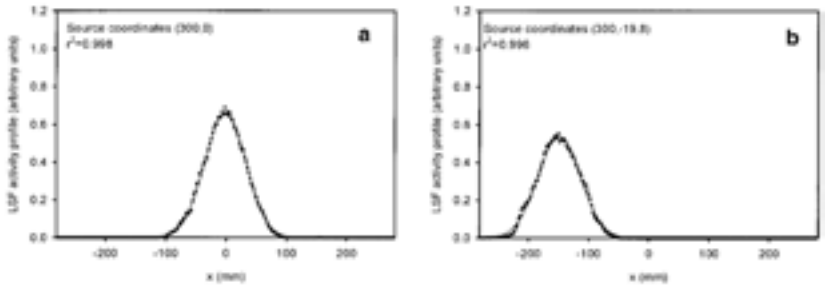

Fig. 4. Experimental (*dots*) and fitted (*solid line*) activity profiles of the LSFs at z=300 mm for θ=0° (**a**) and θ=−19.8° (**b**)

The tails of the collimator response, mainly reflecting photons which have undergone scattering in the collimator, have not been specifically modelled. Our findings on experimental measurements show that the contribution of the tails is about 1% of the total sensitivity. These results are in agreement with those obtained by de Vries et al. [14], which show that septal penetration and scattering in the collimator account for about 5% of the total sensitivity in ^{99m}Tc imaging. The major contribution of this 5% should be located near the central maximum of the collimator-detector response, and as a consequence the contribution of the remaining 4% should be reflected in the parameters of the fitted Gaussian distribution. Thus, these functions may be included in the transition matrix of an iterative reconstruction algorithm in order to correct for variant collimator response.

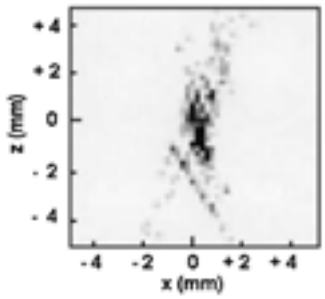

Fig. 5. Two-dimension histogram showing the intersection points of pairs of straight lines passing through the experimental image points and the corresponding source points

Focal region

The measured focal length was F=355 mm, representing an error of 1.43% with respect to the nominal value. The shift was found to be Δx=0.5 mm. This value of Δx was used to correct the co-ordinates of the experimental impacts before obtaining the points of intersection between the pairs of straight lines passing through the source point and their corresponding experimental impact. The points of intersection are plotted in Fig. 5 as a bidimensional histogram, which allows us to assess the collimator convergence. In order to obtain a quantitative measurement of the dispersion of the intersection points, the standard deviations in x- and z-directions of the bidimensional scatter plot were calculated. The results were σ_x=2.5 mm and σ_z=7.1 mm, indicating that the holes are not perfectly focussed on the focal line.

Intrinsic resolution

The measured intrinsic resolution was σ_i=1.7 mm.

Spatial resolution

Once the values of σ for the 42 individual LSFs were obtained, the function (1) was fitted to the data and the

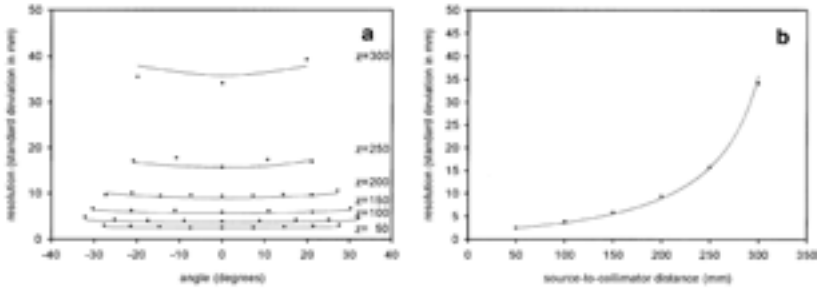

Fig. 6. Experimental (*dots*) and estimated LSF standard deviation (*solid line*) against the source aperture angle (**a**) and against the source-to-collimator distance for the source placed on the axis (θ=0°) (**b**)

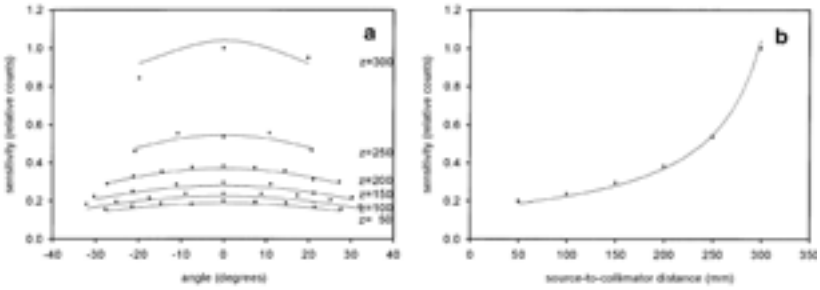

Fig. 7. Experimental (*dots*) and estimated (*solid line*) relative sensitivity against the source aperture angle (**a**) and against the source-to-collimator distance for the source placed on the axis (θ=0°) (**b**)

parameter a was calculated. The best fitting was obtained for a=0.3369 (r^2=0.994). Figure 6a shows the standard deviation σ of the LSFs versus the angle θ for z values from 50 to 300 mm. The circles correspond to the values obtained from the experimental LSFs and the solid lines correspond to the values calculated by using the function (1) with a=0.3369. Figure 6b shows the values of σ versus the z co-ordinate when the source was placed on the axis. As in Fig. 6a, the circles correspond to experimental LSF values and the solid line, to the fitted function (1). Agreement between experimental results and those obtained from function (1) is worth noting and validates the proposed model of the resolution in fan-beam collimators.

Sensitivity

Function (2) was fitted to the 42 sensitivity values, k and n being the constants to be determined. The best fit was obtained for n=1.98 (r^2=0.991), indicating that $\cos^2(\theta)$ is the function which better models the sensitivity dependence on the source angle. Figure 7a shows the sensitivity versus the θ angle for z values from 50 to 300 mm. The circles correspond to the values obtained from the experimental LSFs and the solid lines correspond to the values calculated by using the function (2) with n=2. Figure 7b shows the sensitivity values versus the z co-ordinate when the source was placed on the axis. As in Fig. 7a, the circles correspond to experimental values and the solid line, to the fitted function (2). Disagreement between the predicted and experimental values might be associated with the collimator construction misalignments. The fact that the holes are not focussed on a line affects the quality of the fit. Nevertheless, correlation coefficients are sufficiently high to consider that the detector response is well modelled.

Conclusion

Our findings show differences of 1.43% with respect to the nominal value in the focal length. Dispersion in focal convergence was estimated as 2.5 mm in the x-direction and as 7.1 mm in the y-direction, indicating that the holes are not perfectly focussed on the focal line.

The function derived from geometrical considerations accurately fits the experimental values of the standard deviation of the LSF. The correlation coefficient between the experimental and predicted standard deviations was estimated as 0.994.

As far as the sensitivity is concerned, a simple inverse function allowed us to accurately reproduce the experimental measurements in a wide range of distances from the source to the collimator when the source was located on the z-axis. Our results confirmed that $\cos^2(\theta)$ models accurately the sensitivity dependence on the source angle.

The proposed method may be used to characterise the collimator response so that the correction of the collima-

tor response might be included in iterative reconstruction algorithms.

Acknowledgements. This work was supported in part by the Comisión Interministerial de Ciencia y Tecnología (CICYT-SAF99–0137). The authors thank Mr. M.A. Rodriguez for technical support.

References

1. Hudson HM, Larkin RS. Accelerated image reconstruction using ordered subsets projection data. *IEEE Trans Med Imaging* 1994; 13:601–609.
2. Ros D, Falcón C, Juvells I, Pavía J. The influence of a relaxation parameter on SPECT iterative reconstruction algorithms. *Phys Med Biol* 1996; 41:925–937.
3. Falcón C, Juvells I, Pavía J, Ros D. Evaluation of a cross-validation stopping rule in MLE SPECT reconstruction. *Phys Med Biol* 1998; 43:1271–1283.
4. Moyer RA. A low-energy multihole converging collimator compared with a pinhole collimator. *J Nucl Med* 1973; 15: 59–64.
5. Jaszczak RJ, Chang LT, Murphy PH. Single photon emission computed tomography using multi-slice fan beam collimators. *IEEE Trans Nucl Sci* 1979; 26:610–618.
6. Lim CB, Chang LT, Jaszczak RJ. Performance analysis of three camera configurations for single photon emission computed tomography. *IEEE Trans Nucl Sci* 1980; 27:559–568.
7. Tsui BMW, Gullberg GT, Edgerton ER, Gilland DR, Perry JR, McCartney WH. Design and clinical utility of a fan beam collimator for SPECT imaging of the head. *J Nucl Med* 1986; 27:810–819.
8. Formiconi AR. Geometrical response of multihole collimators. *Phys Med Biol* 1998; 43:3359–3379.
9. Mahowald JL, Robins PD, O'Connor MK. The evaluation and calibration of a fan beam collimator. *Eur J Nucl Med* 1998; 26:314–319.
10. Pareto D, Pavía J, Juvells I, Falcón C, Ros D. Determinación de la distancia focal y evaluación de la convergencia en colimadores de geometría focalizada. *Rev Esp Med Nucl* 1999; 18: 441–444.
11. Nelder JA, Mead R. A simplex method for function minimization. *Comput J* 1965; 7:308–313.
12. Press WH, Teuolsky SA, Vetterling WT, Flanery BP. *Numerical recipes in C, 2nd edn.* Cambridge: Cambridge University Press, 1992.
13. Frey EC, Tsui BMW, Gullberg GT. Improved estimation of the detector response for converging beam collimators. *Phys Med Biol* 1998; 43:941–950.
14. De Vries DJ, Moore SC, Zimmerman RE, Mueller SP, Friedland B, Lanza RC. Development and validation of a Monte Carlo simulation of photon transport in an Anger camera. *IEEE Trans Med Imag* 1990; 9:430–438.

IEEE TRANSACTIONS ON NUCLEAR SCIENCE, VOL. 49, NO. 1, FEBRUARY 2002 17

Geometrical Response Modeling in Fan-Beam Collimators—A Numerical Simulation

D. Pareto, A. Cot, *Member, IEEE*, C. Falcón, I. Juvells, J. Pavía, and D. Ros

***Abstract*—Iterative reconstruction algorithms require modeling of the point spread function (PSF) of the collimator in order to correct the loss of resolution in single photon emission computed tomography (SPECT). A method for modeling the geometric response of a fan-beam collimator is proposed. The geometric PSF is obtained by numerical simulation based on ray-tracing techniques. The versatility of the numerical simulation allows us to generate the array of holes with a distance between them varying as an angular function. This enables us to reproduce the real distribution of holes. The integral of the simulated PSF was calculated in order to determine the relative sensitivity and Gaussian functions were fitted to obtain the resolution. Functions depending on the intrinsic collimator parameters and on the coordinates of the source were fitted to the individual PSF. To validate the functions proposed, a comparison between the predicted values and those obtained from experimental measures was made. Our findings show that the predicted values for relative sensitivity and resolution accurately match the experimental ones, with a correlation coefficient of 0.992 for the sensitivity and 0.994 for the resolution.**

***Index Terms*—Collimator modeling, fan beam, geometric point spread function, ray tracing, single photon emission computed tomography (SPECT).**

I. Introduction

THE collimator response plays a major role in determining resolution in single photon emission computed tomography (SPECT). Iterative reconstruction algorithms allow us to compensate for this loss of resolution by incorporating the distance dependent collimator response into the transition matrix. To this end, the characterization of the collimator response is necessary, especially for fan-beam collimators, which are favored in brain SPECT studies because they offer an adequate tradeoff between resolution and sensitivity.

Manuscript received November 4, 2000; revised June 18, 2001. This work was supported in part by the CICYT(SAF99/0137). The work of D. Pareto was supported by the Universitat Barcelona.

D. Pareto is with Unitat Biofísica i Bioenginyeria, Facultat Medicina, Universitat Barcelona, 08036 Barcelona, Spain. She is also with Servei Medicina Nuclear, Hospital Clínic, 08036 Barcelona, Spain (e-mail: pareto@medicina.ub.es).

A. Cot is with the Department Física i Enginyeria Nuclear, Universitat Politècnica Catalunya, 08028 Barcelona, Spain (e-mail: alberto.cot@upc.es).

C. Falcón is with Unitat Biofísica i Bioenginyeria, 08036 Barcelona, Spain (e-mail: cfalcon@med.ub.es).

I. Juvells is with Lab.Óptica, Dept. Física Aplicada i Óptica, Universitat Barcelona, 08028 Barcelona, Spain (e-mail: ignasi@optica.ub.es).

J. Pavía is with Servei Medicina Nuclear, Hospital Clínic and Institute Investigacions Biomèdiques August Pi i Sunyer (IDIBAPS), 08036 Barcelona, Spain (e-mail: jpavia@clinic.ub.es). He is also with the Institut d'Investigacions Biomèdiques August Pi i Sunyer (IDIBAPS).

D. Ros is with Unitat Biofísica i Bioenginyeria and IDIBAPS, 08036 Barcelona, Spain (e-mail: domenec@medicina.ub.es). He is also with the Institut d'Investigacions Biomèdiques August Pi i Sunyer (IDIBAPS).

Publisher Item Identifier S 0018-9499(02)01637-4.

One method of characterizing fan-beam collimators is to measure the point spread function (PSF) experimentally [1]. However, the experimental setup is onerous and the measurements should be taken over a large number of source positions. Thus, theoretical or, in general, nonexperimental approaches are useful. These approaches have the advantage of being able to predict the sensitivity and resolution of a collimator without prior measurements [2] and are thus helpful in collimator design [3] and iterative reconstruction algorithms [4].

Monte Carlo simulation enables the inclusion of septal penetration and scattering of photons, allowing for complete collimator characterization. Nevertheless, the results obtained using parallel collimators [5] as well as our own results on fan-beam collimators [6] show that for ^{99m}Tc imaging the geometric component accounts for approximately 95% of the total sensitivity, at any source position. These results, although obtained for particular collimator parameters, suggest that the PSF in ^{99m}Tc imaging may be estimated by using the geometrical component.

The theoretical derivation for obtaining a mean geometric PSF in cast converging beam collimators has been described previously [7], [8]. The influence of the discrete nature of the hole array in converging beam collimators has also been studied [9]. In [9], changes in the hole size when moving away from the vertical axis are taken into account and the center-to-center hole distance is considered to be constant.

The aim of this study is: 1) to implement a numerical method of obtaining the geometric PSF in cast fan-beam collimators with hexagonal holes (this method allows the inclusion of changes in the elongation of the hole as well as in the center-to-center hole distance) and 2) to study the changes in the geometric component of the PSF through the collimator field of view in order to determine the range of z values for which sensitivity and resolution may be established as analytical functions of the source coordinates.

II. Materials and Methods

A. Description of the Numerical Method

The fluence of photons at point $P(x, y, -L-B)$ transverse to the detector plane ($z=-L-B$) for a given point source of unit activity located at $P_0(x_0, y_0, z_0)$ is

$$\phi(\mathbf{r}, \mathbf{r}_0, z_0) = \frac{A(\mathbf{r}, \mathbf{r}_0, z_0)}{4\pi\left[(z_0+L+B)^2+|\mathbf{r}-\mathbf{r}_0|^2\right]}\cos\theta' \quad (1)$$

where $\mathbf{r}=(x, y)$ and $\mathbf{r}_0=(x_0, y_0)$ are, respectively, the vectors which describe the position of point P and the orthogonal projection of P_0 on the detector plane, θ' is the angle of P_0P line with respect to the vertical line, L the collimator length,

0018-9499/02$17.00 © 2002 IEEE

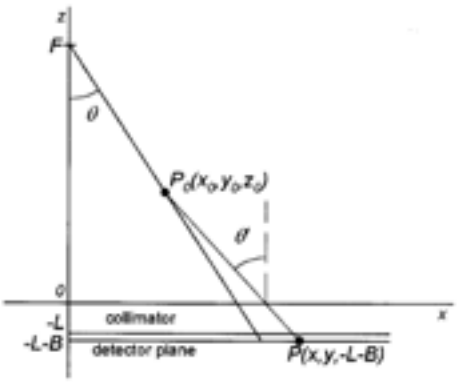

Fig. 1. Collimator scheme showing the parameters used in the text.

B the distance between the back collimator face and the image plane and $A(\mathbf{r}, \mathbf{r}_0, z_0)$ the aperture function of the collimator at point $P(x, y, -L-B)$ (Fig. 1). The factor $1/4\pi$ is the fluence per unit of solid angle; $1/[(z_0+L+B)^2+|\mathbf{r}-\mathbf{r}_0|^2]$ models the decrease with the square of the distance and $\cos\theta'$ describes the changes due to the nonperpendicular incidence of photons on the detector plane.

The algorithm was based on determining the value of $A(\mathbf{r}, \mathbf{r}_0, z_0)$ by scanning the detector plane with a sampling interval $\Delta x = \Delta y = \Delta s$. To this end, we determined whether the ray P_0P passed through a collimator hole ($A = 1$) or not ($A = 0$). The fraction of photons reaching the sampling area in the detector plane for each photon emitted was estimated as: $N(\mathbf{r}, \mathbf{r}_0, z_0) = \phi(\mathbf{r}, \mathbf{r}_0, z_0) \cdot \Delta s \cdot \Delta s$. The PSF was obtained as the bidimensional distribution of $N(\mathbf{r}, \mathbf{r}_0, z_0)$ and the sensitivity was calculated by integrating $N(\mathbf{r}, \mathbf{r}_0, z_0)$ over the entire collimator surface. Given that sensitivity depends on the sampling interval, a study of the changes in sensitivity for different sampling sizes was carried out. The aim was to determine a sampling interval small enough to obtain reliable results but big enough to prevent the computation time from becoming unnecessarily long.

In order to test the algorithm, a hexagonal array with hexagonal holes was considered. We simulated cast collimators constructed with pins of constant hole diameter. The fan-beam collimator parameters were: focal distance $F = 355$ mm, central hole side (i.e., for the hole at $x = 0$, $y = 0$) $w_0 = 0.866$ mm, septal thickness $t_s = 0.2$ mm, length $L = 40$ mm. Thus, the center-to-center distance between the central and the consecutive hole in y direction was $d_y = 1.7$ mm and in x direction $d_x = 2.94$ mm. To generate the hole array pattern, we took into account the fact that fan-beam collimators present a periodic structure along y direction. As a consequence, we only need the information for two consecutive rows (row 1 and row 2) to reproduce the entire array pattern. Thus, six vectors allowed us to reproduce the coordinates and sides of the four holes nearest to $P(x, y, -L-B)$. Four vectors stored the x positions of the hole centers for row 1 and row 2 in the collimator front and back planes, and two vectors stored the hole sides. The x coordinates

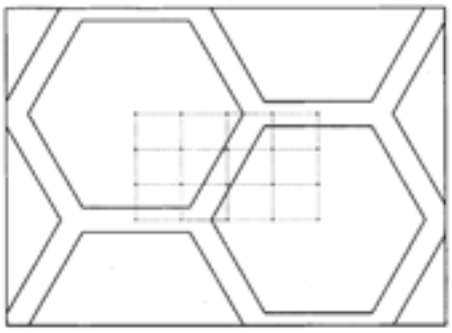

Fig. 2. Detail of the simulated collimator array showing the rectangle of dimensions $[d_y \cdot \cos(30°), d_x/2]$ where the source was located.

X_n of the hole centers and the hole sides in x direction w_n of the collimator right half were obtained by using

$$X_n = X_0 + \sum_{i=0}^{n-1} \frac{d_x}{\cos(\theta_i)}, \qquad n = 1, 2, \ldots \tag{2}$$

$$w_n = \frac{w_0}{\cos(\theta_{n-1})}, \qquad n = 1, 2, \ldots \tag{3}$$

where $X_0 = 0$ for row 1 and $X_0 = d_y \cdot \cos(30°)$ for row 2 and $1/\cos(\theta_i)$ is the elongation factor depending on the angle θ_i between the axis of the ith hole and the vertical line. For the left half of the collimator: $X_{-n} = -X_n$ and $w_{-n} = w_n$. The x, y hole coordinates predicted from (2) were validated from a physical collimator by consecutively measuring distances along the collimator.

Two images were obtained as an output of the program. The first image was the simulated geometric PSF showing the photons that reached the detector plane. The discrete collimator hole structure was visible in this image. The second image was the simulated geometric PSF after convolution with the intrinsic detector response ($\sigma_i = 1.7$ mm). This image reflects the geometric component of the final image obtained throughout the collimator–detector system, which may be compared with the experimental ones.

B. Study of the Individual PSFs

PSF depends on the source coordinates and as a consequence on the position with respect to the collimator hole center. To evaluate the changes in sensitivity, the point source was placed on each of 20 points of a grid of size $d_y \cdot \cos(30°) \times d_x/2$, that is 1.47 × 0.85 mm at the front collimator plane (Fig. 2). Then, sensitivity was calculated for values of z from 50 to 300 mm, scaling the x, y coordinates of the point source in the grid by the factor $(F-z)/F$, where F represents the focal length. The range of z values, in which sensitivity depends on the grid position of the source was determined.

In order to characterize the PSF, we studied the conditions under which a Gaussian distribution fitted the raw data. To this end, PSFs for 24 source locations (Fig. 3) were simulated and Gaussian distributions were fitted by using the Simplex downhill algorithm [10] with the implementation described in [11].

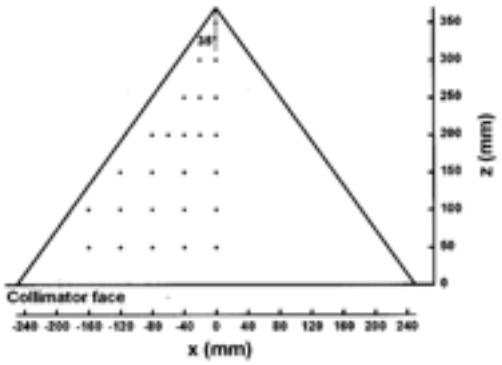

Fig. 3. Positions at which geometrical PSF components were obtained by numerical simulation.

Moreover, we studied the changes in the PSF shape when the source point was displaced along the z axis. To evaluate these changes, the third (bias) and fourth (kurtosi) order moments of the distribution were calculated. The third-order moment of the distribution reflects the asymmetry of the curve, and the fourth-order indicates how near the ratio height/area is to a Gaussian distribution.

C. Description of the Model

Sensitivity of a fan-beam collimator is stated, by using geometric and theoretical approaches [2], [9] as

$$g(z_0,\theta) = k_1 \frac{(F+L)}{(F-z_0)} \cos^n \theta \tag{4}$$

where k_1 is the sensitivity factor, which depends on the intrinsic collimator parameters. As indicated above, F is the focal distance, L is the collimator length, and z_o is the height of the point source. The angle θ is the source aperture angle defined as the angle between the z axis and the straight line passing through the point source and through the point in the focal line with the same y coordinate as the point source (see Fig. 1). Thus, $\cos^n \theta$ is the angular dependence. Values of $n = 2$ [2], [12] and $n = 1$ [9] have been reported. We studied this angular dependence to obtain the applicability conditions of each function.

If we assume that Gaussian distributions accurately fit the individual PSFs in a range of z values, then the resolution may be estimated by the standard deviation of the Gaussian. Following the geometric arguments described in [1], it is assumed that the standard deviation in the x direction σ_{xc} is proportional to the maximum distance reached in the image plane by the photons emitted at the point source $P_0(x_0, y_0, z_0)$

$$\sigma_{xc}(z_0,\theta) = k_2 \frac{(z_0+L+B)w_0(2F+L)}{\sqrt{L^2(F-z_0)^2 - w_0^2(L+2z_0)^2}} \frac{1}{\cos\theta}. \tag{5}$$

So as to include the detector response, we assumed that the intrinsic resolution was a Gaussian distribution. The convolution with the geometric collimator response was then performed. Since the convolution of two Gaussian distributions is also a Gaussian distribution, the total spatial resolution was then obtained as

$$\sigma_x(z_0,\theta) = \sqrt{\sigma_i^2 + \sigma_{xc}^2(z_0,\theta)}. \tag{6}$$

Along the y-direction, the collimator configuration is parallel. Thus, taking $F \to \infty$, the standard deviation can be obtained

$$\sigma_{yc}(z_0,\theta) = k_3 \frac{(z_0+L+B)\cdot 2\cdot w_0}{L} \tag{7}$$

$$\sigma_y(z_0,\theta) = \sqrt{\sigma_i^2 + \sigma_{yc}^2(z_0,\theta)}. \tag{8}$$

To determine k_1, k_2 and k_3, (4), (6), and (8) were fitted to values of sensitivity, σ_x and σ_y obtained from the 24 simulated PSFs. In order to assess the quality of the fit, the coefficient of determination (r^2) was employed. This coefficient is defined as the square of the correlation coefficient between the values at the individual points and those obtained by using the fitting function, respectively. The standard error was used to assess the uncertainty of the estimated parameters.

D. Experimental Measurements

Experimental measures were carried out to validate the numerical simulation and the analytic functions for sensitivity and resolution. A capillary of 60 mm length and 1.1-mm internal diameter filled with 25 MBq of ^{99m}Tc was employed. Acquisitions were done with a double-headed Helix (Elscint, Haifa) gamma camera using cast collimators (Van Mullekon, Holland) with field of view of 530 × 250 mm. The actual fan-beam parameters were focal $F = 355$ mm [1], hole side $w_0 = 0.866$ mm, septal distance $s = 0.2$ mm, length $L = 40$ mm and distance between the back collimator face and the image plane $B = 8$ mm. The capillary was placed at the same positions as those used in simulation (see Fig. 3) and in symmetric positions with respect to the z axis. Thus, 42 measurements were taken, between $z = 50$ mm and $z = 300$ mm for height and $\theta = -32°$ to $\theta = 32°$ for the aperture angle. Values obtained from the symmetric positions were averaged in order to diminish local errors.

To evaluate the quality of predicted values of sensitivity and resolution with respect to experimental values, the coefficient of determination (r^2) and the mean relative error (ε) were employed. The error ε is the mean of relative residuals between predicted and experimental sensitivities and standard deviations.

III. Results and Discussion

A. Numerical Method

The accuracy with which the PSF is obtained depends on the interval size employed when scanning the detector plane. A size that is too small results in an unnecessary increase in computation time. Thus the most suitable size of the sampling interval, Δs, should be determined. For this purpose the detector plane was scanned by using values (in mm) of 0.005, 0.01, 0.02, 0.04, 0.06, 0.08, 0.10 for Δs. The sensitivity was obtained as the integral of the simulated geometric component of the PSF. Fig. 4 shows the relative error in sensitivity calculation as a function of the sampling interval. This error was quantified as the relative error in sensitivity obtained by using the different values of Δs with respect to the value obtained with $\Delta s = 0.005$ mm. The

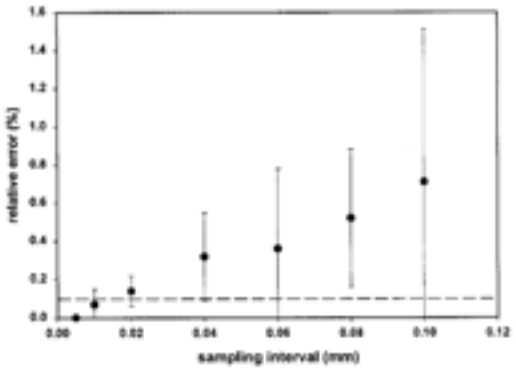

Fig. 4. Error in sensitivity calculation as a function of the sampling interval. The error is calculated as the relative error in the sensitivity values with respect to those obtained with $\Delta s = 0.005$ mm. Mean and standard deviations over 80 source locations are plotted. The dashed line indicates an error of 0.1%.

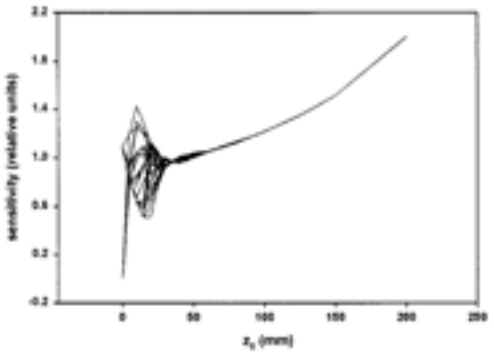

Fig. 5. Sensitivity as a function of the z coordinate for the source positions of Fig. 2. Values are relative to the value obtained for a point source located at $P_0(0, 0, 50)$.

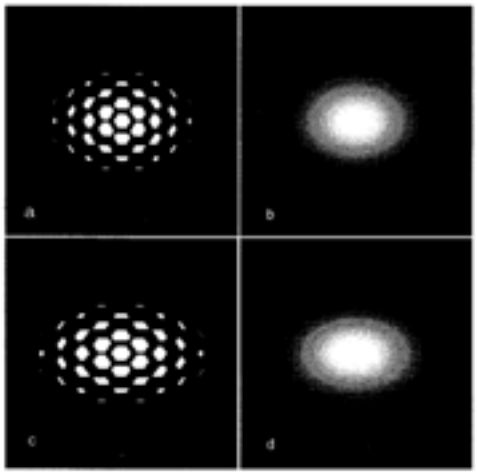

Fig. 6. (a) Simulated geometric component of PSF for a point source placed at $P_0(0, 0, 100)$ and (c) $P_0(160, 0, 100)$. Images before (a) and (c) and after (b) and (d) convolution with the intrinsic detector response are shown.

mean sensitivity values and standard deviations over 80 point source locations are plotted. The 80 points correspond to the 20 positions of Fig. 2 for point sources located at 50, 100, 200, and 300 mm above from the collimator front plane.

We can observe that the mean error for $\Delta s = 0.01$ mm is less than 0.1% and the maximum error was 0.2%. Thus, this sampling interval allows for a good compromise between accuracy and computing time and in order to save computing time, we chose $\Delta s = 0.01$ as the value to be used. Nevertheless, as we can see from Fig. 4, sampling intervals of 0.02 or 0.04 mm could be used if errors less than 1% were acceptable.

Other simulation parameters were: image size 1024×1024 and a pixel size of 0.55 mm. This selection was made in order to approximate as closely as possible to a continuum. The image was then convoluted with the intrinsic detector response and zoomed to 256×256 pixels to simulate the experimental conditions. With the parameters employed, the computer time ranged between 10 s (for $z = 50$ mm) and 12 min (for $z = 300$ mm) in a HP-Apollo9000-C160 workstation.

B. Individual PSFs

Fig. 5 shows the collimator sensitivity as a function of the source height for the 20 source positions indicated in Fig. 2. We can observe considerable changes in the sensitivity depending on source position for $z < 50$ mm, whereas no significant changes appear above this height.

Fig. 6 shows the geometric collimator response for a point source located at $z = 100$ mm and $\theta = 0°$ (top) and $\theta = 32°$ (bottom). On the left-hand side, the images of the collimator response show the discrete nature of the array pattern. On the right, we can see the geometric PSFs after the intrinsic detector resolution has been incorporated. The comparison of top and bottom images shows an increased size of the PSF in z direction as predicted by (5) and (6), whereas no changes appear in direction, due to the parallel structure of the holes in this direction.

The simulated geometric PSFs, once the detector response was included, were integrated over the x- and y directions in order to determine how well an unidimensional Gaussian distribution fitted the collimator–detector response in the two directions. Fig. 7 plots these functions (dots and triangles) and the fitted Gaussian (solid line) for the PSFs of Fig. 6, i.e., when the source point was located at $P_0(0, 0, 100)$ and $P_0(160, 0, 100)$. The results obtained were $\sigma_x = 3.72$ mm, $\sigma_y = 2.86$ mm, coefficient of determination $r^2 = 0.998$, and $\sigma_x = 4.26$ mm, $\sigma_y = 2.86$ mm with $r^2 = 0.999$, respectively. These results support quantitatively the close match between the simulated and fitted functions shown in Fig. 7. The mean and standard deviation of r^2 for the 24 fittings was 0.999 ± 0.001.

Although these results indicate that Gaussian distributions accurately fit the simulated PSFs, the values of the third moment showed a slight bias when the coordinate and aperture angle of the source increase. Fig. 8 shows the bias as a function of the aperture angle for z coordinates of the source between 50 and 300 mm. We can observe a linear increase in bias with the aperture angle. The slope of the linear function increases with z.

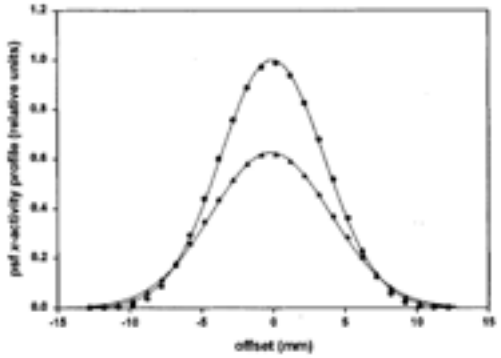

(a)

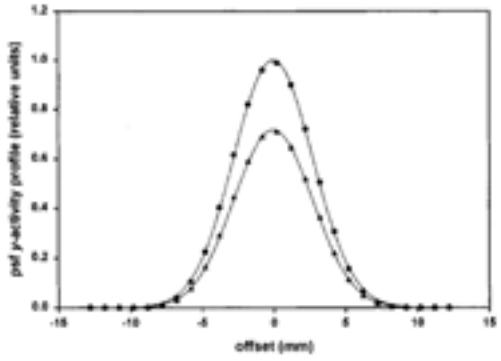

(b)

Fig. 7. (a) Profiles in x direction and (b) y direction obtained after collapsing the simulated PSFs of Fig. 6, corresponding to a point source located at $P_0(0, 0, 100)$ (circles) and $P_0(160, 0, 100)$ (triangles). Fitted Gaussian distributions (solid line) are also shown. A value of 1 has been assigned to the maximum in the two graphs.

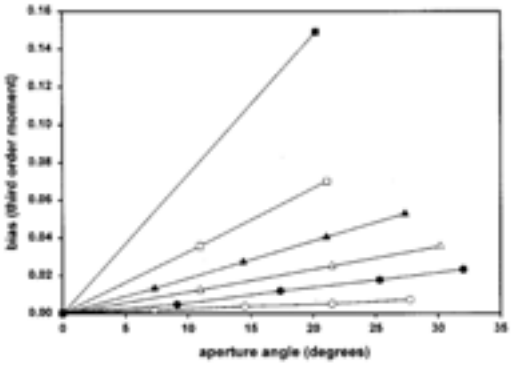

Fig. 8. Bias of simulated PSFs versus aperture angle of source, θ, at z = 50 mm (hollow circles), z = 100 mm (black circles), z = 150 mm (hollow triangles), z = 200 mm (black triangles), z = 250 mm (hollow squares) and z = 300 mm (black squares). The solid straight lines, which cross on the different symbols, show the linear dependence between bias and aperture angle.

The kurtosi decreases with height but remains almost constant with respect to the aperture angle. The mean and standard deviation for kurtosi varies from 2.90 ± 0.00 for $z = 50$ mm to 2.62 ± 0.00 for $z = 300$ mm. These results confirm that the simulation program is accurate enough for detecting slight asymmetries in the response that one would expect to find when the source moves away from the z axis. Likewise, bias values are sufficiently low and kurtosi is sufficiently close to that of a Gaussian distribution to justify the high values of the coefficient of determination obtained in the fitting. These findings provide evidence that the geometric component of the PSF once it has been convolved with the detector response can be regarded as a Gaussian distribution.

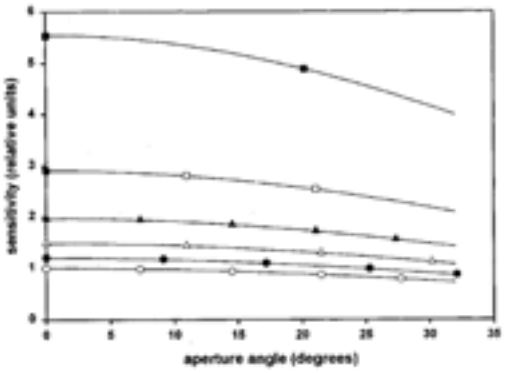

(a)

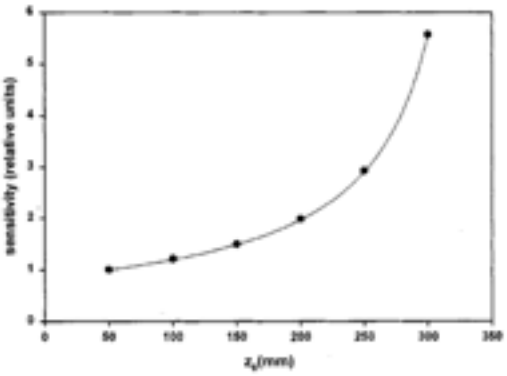

(b)

Fig. 9. (a) Sensitivity as a function of the source aperture angle at z = 50 mm (hollow circles), z = 100 mm (black circles), z = 150 mm (hollow triangles), z = 200 mm (black triangles), z = 250 mm (hollow squares) and z = 300 mm (black squares). (b) Sensitivity is plotted as a function of the z-coordinate for a source point located on the z-axis. The solid lines correspond to the fitted function $g(z_0, \theta)$ from (4). Values are relative to the value obtained for a point source located at $P_0(0, 0, 50)$.

C. The Model

The fitting of (4) to the set of 24 sensitivity values from simulated PSFs resulted in $n = 2.000 \pm 0.017$ with $r^2 = 0.999$. Fig. 9 shows the dependence of sensitivity on the aperture angle and the z coordinate of the source. In the upper graph the solid lines correspond to the values obtained from (4) with $n = 2$. Sensitivity as a function of the z coordinate of the point source

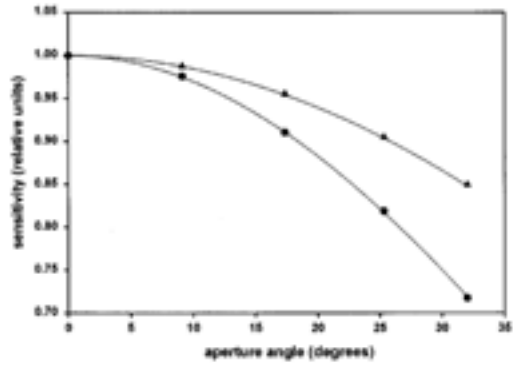

Fig. 10. Sensitivity as a function of the aperture angle of a source located at $z = 100$ mm for an equidistant (black triangles, in solid line $\cos\theta$ function) and a nonequidistant collimator array (black circles, in dotted line $\cos^2\theta$ function). A value of 1 has been assigned to the maximum.

is shown at the bottom of Fig. 9. Values in both graphs are normalized by the value obtained for $P_0(0.\ 0.\ 50)$. We can observe the good match between the values obtained from the individual simulated geometric PSFs and those obtained from (4). The high coefficient of determination indicates that the proposed model accurately predicts the sensitivity in the range of heights [50, 300] mm. Our findings in Fig. 5 indicate that below $z = 50$ mm, sensitivity depends on the exact source coordinates and (4), which does not take into account these changes, is not suitable for predicting the individual PSF. Nevertheless, if we consider that the source corresponds to a continuous distribution of activity, (4) may be employed to extrapolate an averaged PSF in iterative reconstruction algorithms.

We have confirmed that sensitivity dependence on $\cos\theta$ or $\cos^2\theta$ was related to the center-to-center distance. Thus, sensitivity depends on $\cos^2\theta$ when the center-to-center distance varies as $1/\cos\theta$. Nevertheless, if the distance between centers is constant, the angular dependence is $n = 1$. This can be seen in Fig. 10, where for a point source at $x = 100$ mm, the sensitivity is shown as a function of the aperture angle when the center-to-center distance remains constant along the x coordinate of the collimator (triangles) and when it varies as $1/\cos\theta$ (circles). Solid lines correspond to the $\cos\theta$ and $\cos^2\theta$ functions. We can see the match between these functions and the geometric PSF sensitivity obtained by using each hypothesis.

As indicated above, the 24 simulated PSFs were integrated over the x and y directions. Gaussian distributions were fitted to these raw data and standard deviations σ_x and σ_y were obtained as a measure of resolution. Equation (6) was fitted to the σ_x values obtained in the simulated PSFs. A value of $k_2 = 0.345 \pm 0.001$ was obtained as a result of the fitting and the coefficient of determination was found to be $r^2 = 0.999$.

When (8) was fitted to the σ_y values, we found $k_3 = 0.347 \pm 0.001$ and $r^2 = 0.998$.

The upper graph in Fig. 11 shows the values of σ_x as a function of the aperture angle for values of z between 50 and 300 mm. As expected, no changes with respect to the aperture angle were observed in σ_y. The lower graph in Fig. 11 shows

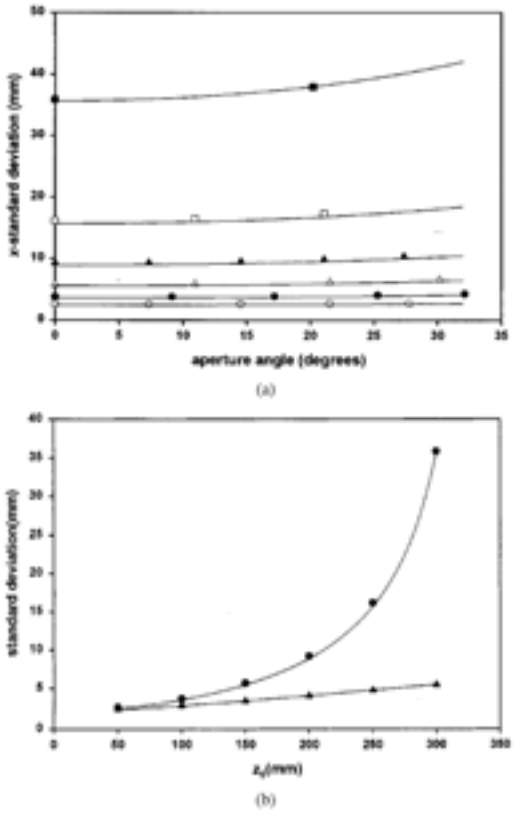

Fig. 11. (a) Standard deviation in x direction as a function of the source aperture angle at [$z = 50$ mm (hollow circles), $z = 100$ mm (black circles), $z = 150$ mm (hollow triangles), $z = 200$ mm (black triangles), $z = 250$ mm (hollow squares) and $z = 300$ mm (black squares)]. (b) Standard deviation in x-direction, (circles) and y-direction (triangles) as a function of the z coordinate for a source point located on the z axis. The solid lines correspond to the fitted functions $\sigma_x(z_0.\ \theta)$, $\sigma_y(z_0.\ \theta)$ from (6) and (8).

the values of σ_x and σ_y as a function of the z coordinate of the source. We can observe important differences between σ_x and σ_y when z increases and approximates to the collimator focal line. The close match between the predicted (solid line) and the individual values obtained from the simulated geometric PSF component is worth noting.

D. Experimental Measurements

Finally, the capability of our model to reproduce experimental values was evaluated. Fig. 12 shows the profiles in x direction after collapsing the simulated (solid line) and experimental (symbols) PSFs for source points located at different places in height on z axis (a) and out of z axis (b). The good agreement between profiles of simulated and experimental PSFs is worth noting.

In order to compare quantitative values, Table I shows the standard deviation for the profiles of Fig. 12. The results of Table I confirm the visual assessment from Fig. 12. Discrepan-

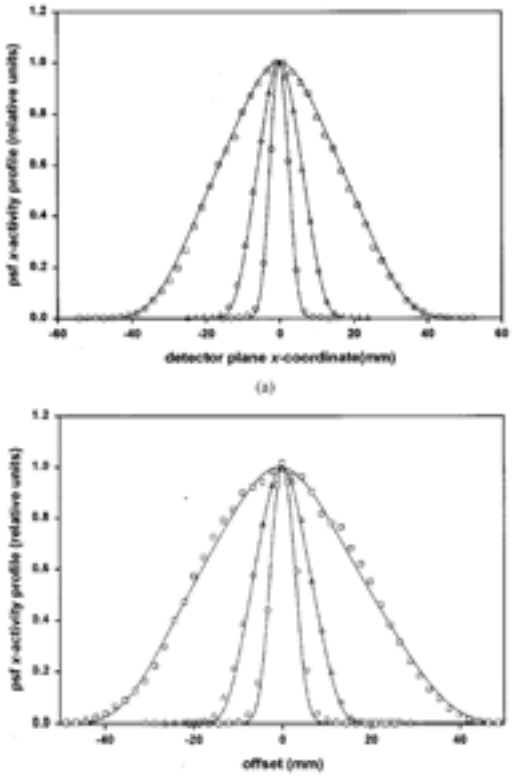

Fig. 12. Profiles in x direction obtained from collapsed simulated (solid line) and experimental PSFs (symbols) for source points located on (a) z axis at $P_0(0,\ 0,\ 50)$ (circles), $P_0(0,\ 0,\ 150)$ (triangles), $P_0(0,\ 0,\ 250)$ (squares) and (b) outside z axis at $P_0(-160,\ 0,\ 50)$ (circles), $P_0(-120,\ 0,\ 150)$ (triangles), $P_0(-40,\ 0,\ 250)$ (squares) from right to left, respectively. A value of 1 has been assigned to the maximum of each profile in the two graphs.

TABLE I
EXPERIMENTAL (σ_{ex}) AND CALCULATED (σ_c) STANDARD DEVIATIONS IN x DIRECTION

x_0z_0 (mm)	(0,50)	(0,150)	(0,250)	(160,50)	(120,150)	(40,250)
σ_c (mm)	2.47	5.60	16.07	2.66	6.51	17.17
σ_{ex} (mm)	2.45	5.84	15.81	3.01	6.70	17.20
σ_c/σ_{ex}	1.01	0.96	1.02	0.88	0.97	1.00

cies between experimental and calculated standard deviations, might be explained by taking into account that holes were not perfectly focused on the focal line [1].

Table II shows the absolute experimental and calculated geometric sensitivities. The results of calculated sensitivity correspond to the simulated geometric component after correction by the detector absolute efficiency. We can see that the geometric component represents, on average, about 96% of the total sensitivity. These results are in agreement with those obtained by Monte Carlo simulation [5], [6], which estimates geometric contribution to be about 95%, septal penetration to be 4% and coherent scattering to be 1%, the incoherent scattering being negligible with 0.1%. The small differences between experimental and calculated geometric sensitivities at points $P_0(120,\ 150)$ and $P_0(40,\ 250)$ could be due to a nonperfect focusing of holes on the focal line in this region [1].

TABLE II
ABSOLUTE EXPERIMENTAL (S_{ex}) AND CALCULATED* (S_c) SENSITIVITIES

x_0z_0 (mm)	(0,50)	(0,150)	(0,250)	(160,50)	(120,150)	(40,250)
S_c (x10^{-5})	6.12	9.18	17.95	4.76	6.87	15.71
S_{ex} (x10^{-5})	6.50	9.81	18.72	5.08	6.92	15.79
S_c/S_{ex}	0.94	0.94	0.96	0.94	0.99	0.99

*Calculated sensitivities correspond to the geometric component corrected by the absolute efficiency of the detector.

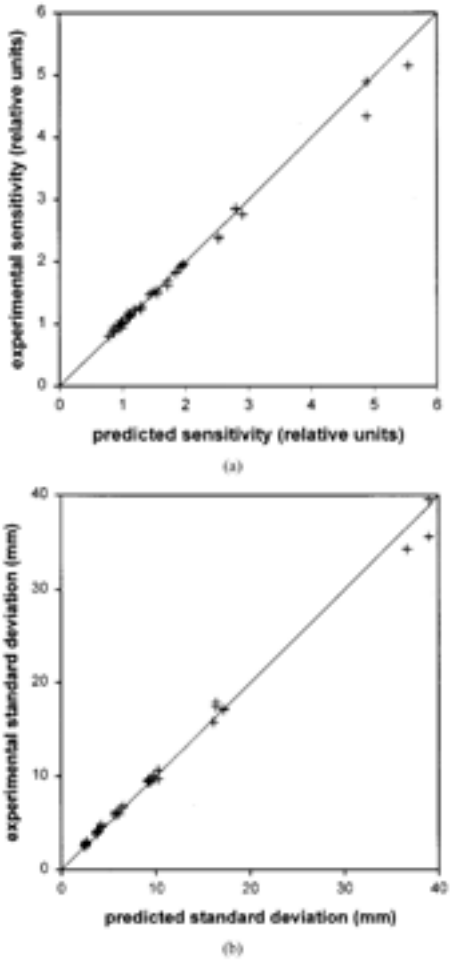

Fig. 13. Experimental values of (a) sensitivity and standard deviation versus (b) the values predicted by the model proposed.

For a complete comparison, Fig. 13 shows experimental relative sensitivity and standard deviation in x direction versus the predicted values obtained from (4) and (6). The upper graph

shows the experimental versus the predicted sensitivity values. The identity line is also displayed. Values in both axes are relative to the sensitivity for a point source located at $P_0(0, 0, 50)$. A coefficient of determination of $r^2 = 0.992$ was found between the two sets of values (mean error em% 0.25 ± 4.19). Because relative sensitivity is used in iterative reconstruction algorithms, these results indicate that the model represented by (4) may be employed in these algorithms.

The lower graph in Fig. 13 plots the experimental versus predicted standard deviation. Given that experimental measurements were obtained from a capillary placed in a direction parallel to the focal line, only values of σ_x were evaluated. In this case, the correlation coefficient was $r^2 = 0.994$ and the mean error and standard deviation were 3.33 ± 4.69 (in%). The mean error of 3.33% might be an estimate of the effect of septal penetration and scatter on resolution, although further investigation using Monte Carlo simulation should be done for validation. The agreement observed in Fig. 13 between the predicted and the experimental values for sensitivity and resolution indicates that the analytic functions (4) and (6) are advisable for use in real fan-beam cast collimators.

IV. Conclusion

The agreement between the simulated and the experimental values for relative sensitivity and resolution demonstrates the validity of the numerical method implemented in the study of $^{99\,m}$Tc imaging through typical fan-beam collimators such as those we have employed. The algorithm is well adapted for obtaining PSF in cast fan-beam collimators, as no hypothesis about array periodicity is necessary. The method can be adapted to different array geometry and hole shapes. Thus, we have demonstrated that sensitivity varies as a $\cos^2\theta$ factor when the center-to-center distance varies as $1/\cos\theta$ and as a $\cos\theta$ factor when this distance is constant.

The analytical functions modeling sensitivity and resolution accurately predict both the simulated and the experimental values, for the simulated collimator, when the source–collimator distance is greater than 50 mm. Below this height, sensitivity is highly dependent on the source position and small displacements in the x or y coordinates bring about considerable changes. In this situation, the analytical functions that we have employed are not suitable for predicting the individual PSF for a point source at $P_0(x_0, y_0, z_0)$ although they may be used to obtain an averaged PSF around this point in iterative reconstruction algorithms.

References

[1] D. Pareto, J. Pavía, C. Falcón, I. Juvells, A. Cot, and D. Ros, "Characterization of fan-beam collimators," *Eur. J. Nucl. Med.*, vol. 28, pp. 144–149, 2001.

[2] C. B. Lim, L. T. Chang, and R. J. Jaszczak, "Performance analysis of three camera configurations for single photon emission computed tomography," *IEEE Trans. Nuc. Sci.*, vol. NS-27, pp. 559–568, 1980.

[3] P. Gantet, J. P. Esquerré, B. Danet, and R. Gairaud, "A simulation method for studying scintillation camera collimators," *Phys. Med. Biol.*, vol. 35, pp. 659–669, 1990.

[4] A. R. Formiconi, A. Passeri, and P. Calvini, "Theoretical determination of the collimator geometrical transfer function for the reconstruction of SPECT data," *IEEE Trans. Nucl. Sci.*, vol. 46, pp. 1075–1080, Aug. 1999.

[5] D. J. De Vries, S. C. Moore, R. B. Zimmerman, S. P. Mueller, B. Friedland, and R. C. Lanza, "Development and validation of a Monte Carlo simulation of photon transport in an Anger camera," *IEEE Trans. Med. Imaging*, vol. 9, pp. 430–438, 1990.

[6] A. Cot, D. Pareto, J. Sempau, S. Bullich, J. Pavía, F. Calviño, and D. Ros, "Evaluation of geometric, scatter and septal penetration components in fan-beam collimators using Monte Carlo simulation," *IEEE Trans. Nucl. Sci.*, vol. 49, pp. 12–16, Feb. 2002.

[7] W. Tsui and G. T. Gullberg, "The geometric transfer function for cone and fan-beam collimators," *Phys. Med. Biol.*, vol. 35, pp. 81–93, 1990.

[8] E. C. Frey, B. M. W. Tsui, and G. T. Gullberg, "Improved estimation of the detector response function for converging beam collimators," *Phys. Med. Biol.*, vol. 43, pp. 941–950, 1998.

[9] A. R. Formiconi, "Geometrical response of multihole collimators," *Phys. Med. Biol.*, vol. 43, p. 3359, 1998.

[10] J. A. Nelder and R. Mead, "A simplex method for function minimization," *Comput. J.*, vol. 7, pp. 308–313, 1965.

[11] W. H. Press, S. A Teulosky, W. T. Vetterling, and B. P. Flanery, *Numerical Recipes in C*, 2nd ed. Cambridge, U.K.: Cambridge Univ. Press, 1992.

[12] R. A. Moyer, "A low-energy multihole nonverging collimator compared with a pinhole collimator," *J. Nucl. Med.*, vol. 15, pp. 59–64, 1974.

Iterative reconstruction with compensation of the spatial variant fan-beam collimator response in neurotransmission SPET imaging

D. Pareto, A. Cot, J. Pavía, C. Falcón, I. Juvells, F. Lomeña, D. Ros

Abstract-- **The dopamine transporter (DAT) has been shown to be a sensitive indicator of nigrostriatal dopamine function. Although visual inspection is often sufficient to assess DAT imaging, quantification could improve the diagnosis accuracy of SPET studies of the dopaminergic system. The aim of the present study was to assess the accuracy of quantification of the striatal/background uptake ratio when correction of attenuation, scatter and spatially variant fan-beam collimator response are included in iterative algorithms.**

A numerical striatal phantom was implemented and simulated projections were obtained by using the SimSET Monte Carlo code. Ordered Subsets Expectation Maximisation algorithm (OSEM) was employed in reconstruction. Our results show that the inclusion of the spatially variant PSF in the transition matrix results in an improvement in the calculated striatal/background uptake ratio of 8% in putamen and 16% in caudate. Improvement was 30 % in putamen and 43 % in caudate when correction of attenuation, scatter and spatially variant collimator response were included in the reconstruction.

Key Words: SPET, fan-beam collimator, OSEM, neurotransmission imaging.

I. INTRODUCTION

Following the advances in molecular imaging, neurotransmission SPET has become an important field in neuroimaging and is today regarded as a useful tool in clinical [1,2] and basic research [3]. There are two important reasons for this: 1) it has so far not been able to image neurotransmission *in vivo* by means other than PET or SPET, and 2) SPET is a widely accessible and cost-efficient technique. Despite controversy about whether or not SPET imaging of dopamine uptake sites can replace PET imaging in neurological disorders [4,5], some authors support the view that at least in clinical settings SPET imaging can replace PET imaging of the presynaptic dopaminergic function in Parkinson's disease (PD) [4].

Presynaptic dopaminergic function is associated with the dopamine transporter (DAT). The DAT re-uptakes dopamine from the synaptic cleft and has been shown to be a sensitive indicator of nigrostriatal dopamine function. Dysfunctions of the presynaptic dopaminergic system are involved in PD and, as a consequence, DAT imaging is a useful tool to confirm or exclude PD [1, 6]. A number of cocaine analog SPET agents which bind to DAT sites have been developed [1]. These analogues include ^{123}I agents, such as the recent and available FP-CIT [7], and ^{99m}Tc agents [8,9].

Although visual inspection is often sufficient to assess DAT imaging, quantification might improve the diagnostic accuracy of SPET studies of the dopaminergic system [10-12]. In particular, quantification of dopamine transporter SPET studies in PD could help us to diagnose PD in the early pre-clinical stages [13,14], to follow and measure the progression of disease [13-16], and to assess the effects of potential neuroprotective treatment strategies [17].

Recent advances in SPET technology have considerably improved possibilities of quantification in nuclear neuroimaging. On the one hand, fan-beam collimators on multi-head systems offer a good trade-off between resolution and noise. On the other hand, transmission imaging systems, which enable us to obtain attenuation maps, are now available. Moreover, iterative reconstruction algorithms may further improve resolution and allow for a more reliable quantification. These algorithms permit modelling of the projection process, allowing for correction of attenuation and spatially variant collimator response in the reconstruction process. Finally, the introduction of the Ordered Subsets Expectation Maximisation algorithm (OS-EM) [18] has allowed us to reconstruct images within an acceptable time.

The aim of the present study was to assess the improvement in accuracy of quantification of the striatal/background ratio in SPET neurotransmission ligand imaging when correction of attenuation, scatter and spatially variant fan-beam collimator response are included in iterative algorithms. Attenuation and scatter are, in general, thought to

This work was supported in part by the CICYT(SAF99/0137). D.Pareto is founded by Universistat Barcelona.

D.Pareto is with Unitat Biofísica i Bioenginyeria, Facultat Medicina, Universitat Barcelona, Casanova 143, 08036 Barcelona, SPAIN (e-mail: pareto@medicina.ub.es) and Servei Medicina Nuclear, Hospital Clinic, Villarroel 176, 08036 Barcelona, SPAIN.

A.Cot is with Dept.Física i Enginyeria Nuclear, Universitat Politècnica Catalunya, Barcelona, SPAIN (e-mail: alberto.cot@upc.es).

J.Pavía and F.Lomeña are with Servei Medicina Nuclear, Hospital Clinic and Inst. Investigacions Biomèdiques August Pi i Sunyer (IDIBAPS), Barcelona, SPAIN (e-mail: jpavia@clinic.ub.es).

C.Falcón is with Unitat Biofísica i Bioenginyeria and Serveis Científico Tècnics (SCT) (e-mail: cfalcon@med.ub.es).

I.Juvells is with Lab.Óptica, Dept.Física Aplicada i Óptica, Universitat Barcelona, SPAIN (e-mail: ignasi@optica.ub.es).

D.Ros is with Unitat Biofísica i Bioenginyeria and IDIBAPS (e-mail: domenec@medicina.ub.es).

be the most important effects. Nevertheless in this case, where small structures such as caudate and putamen are involved in quantification, correction of the variant point spread function (PSF) can play a significant role.

II. Materials and Methods

A. Numerical phantom

A numerical phantom was implemented by using experimental data obtained from a CT image of an anthropomorphic striatal phantom (Radiology Support Devices, RSD, Inc., Long Beach, CA). Thirty-two axial slices throughout the whole physical phantom, 128x128 pixels each, were acquired. CT image was segmented in order to obtain brain tissue, basal ganglia and bone. Brain tissue and bone were automatically segmented by thresholding the CT image. Striatal cavities were manually traced over the eight corresponding slices of the CT image.

The activity distribution was generated by setting a constant value for all basal ganglia and a lower constant value for the rest of the brain. Ratios of 7/1, 5/1, 3.5/1 for striatum to background uptake were established, thereby simulating normal and pathologic situations.

The non-uniform attenuation map was obtained by setting the attenuation coefficients to 0.014 mm^{-1} for brain and 0.029 mm^{-1} for bone. Figure 1 shows one section of the activity distribution where we can see the caudate and putamen basal ganglia and the corresponding attenuation map.

Figure 1. Activity and attenuation distributions in one section of the striatal phantom. Caudate and putamen basal ganglia can be observed in the activity image.

B. Projections

The SimSET Monte Carlo code [19] was employed to simulate SPET projections. The simulation conditions are described below:

a. The photon history generator module included: 1) the numerical phantom described above with a voxel size of 1.7x1.7x5.0 mm^3 2) tracking of 500 million photons to obtain approximately 3.5 million detected photons in projections, thus mimicking real studies obtained with a dual-head gammacamera, 3) a rotation radius of 140 mm, 4) photon energy of 159 keV, corresponding to the main emission of ^{123}I. No contamination of high energy photons was considered for ^{123}I. Ten noise runs were carried out to statistically assess the influence of noise.

b. The binning module included: 1) 120 projections over 360^o, 128x32 pixels each, pixel size 4.4x4.4 mm^2, 2) an energy window selecting photons ranging from 143 to 175 keV, 3) collection of scattered and primary photons in separate files.

c. The collimator module incorporated a converging fan-beam cast collimator with focal distance F=355 mm, hole side w=0.866 mm, septal thickness t_s=0.2 mm, length L=40 mm, distance from the back collimator plane to the detector plane B=8mm and field of view (FOV) of 530x250 mm.

d. The detector module included a NaI detector. The intrinsic energy resolution function was modelled as a Gaussian distribution with FWHM of 11 % for 159 keV.

C. Reconstrucion

Ordered Subsets Expectation Maximisation (OSEM) [18] was employed in reconstruction. Six subsets and 1 to 32 iterations were used. Ordering of subsets was established in such a way that each subset included the most independent information available and new independent information was introduced in successive subsets. The reconstruction parameters were 128x128 matrix size and 1.9 mm pixel size. Attenuation correction was performed in the reconstruction process by including the non-uniform attenuation map described above in the projector/backprojector pair.

Scatter correction is an important subject and a number of methods have been proposed and evaluated [20,21]. Nevertheless, this study is focused on evaluating the effect of the correction of degradations on reconstruction rather than studying the most reliable method of scatter correction. Thus, the ideal correction was considered to correct projections for scattered photons. To this end, only primary photons which had not undergone scatter were considered from SimSET.

Correction of collimator/detector response was carried out by modelling the spatially variant resolution and sensitivity and by including these functions in the transition matrix [22]. Earlier results obtained by using Monte Carlo techniques [23] show that although the absolute sensitivity values (including primary, septal penetration and scattered photons) differ from those corresponding to only primary photons, the ratio primary photons/total photons is almost constant. Thus, the relative sensitivity function can be obtained directly from the primary photons.

The relative sensitivity was obtained as the sensitivity values for each source position with respect to the sensitivity at z=50 mm, which was taken as a reference [22,24]:

$$s(z,\theta) = \frac{(F-50)}{(F-z)}\cos^2\theta \qquad (1)$$

where F is the focal length, z is the vertical distance from the source point to the front plane of the collimator and θ is the angle between the normal and the straight line passing through the source point and the focal line. All distances are in mm.

The resolution was estimated as the standard deviation of a Gaussian distribution [22,24]:

$$\sigma(z,\theta) = \sqrt{\sigma_i^2 + \left(\frac{0.3369\cdot w\cdot(z+L+B)\cdot(2F+L)}{\sqrt{L^2\cdot(F-z)^2 - w^2\cdot(L+2z)^2}}\cdot\frac{1}{\cos\theta}\right)^2} \qquad (2)$$

where σ_i and σ_c are respectively the intrinsic resolution and collimator response, and all other parameters have been described above. The measured intrinsic resolution was σ_i = 1.7mm.

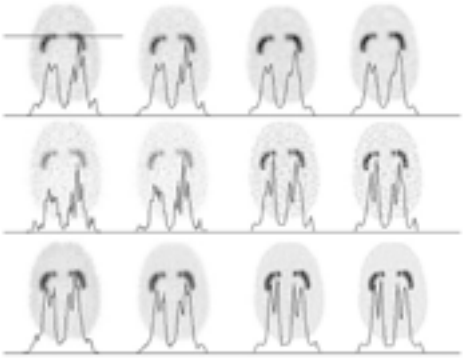

Figure 2. Reconstructed images after 5 iterations (top), 30 iterations (middle) for 3.5 million counts in projections and after 30 iterations for 35 million counts (bottom). Columns show images reconstructed without corrections (AnCnSn), with only attenuation correction (AyCnSn), with attenuation and collimator response correction (AyCySn) and with attenuation, collimator response and ideal scatter correction (AyCySy). The graphs represent the activity profiles along the horizontal line indicated in the top left image.

Different reconstructions were performed: 1) without corrections, *i.e* no attenuation correction, no collimator/detector response correction, and no scatter correction (AnCnSn), 2) with attenuation correction (AyCnSn), 3) with attenuation and collimator response correction (AyCySn), 4) with attenuation, collimator response and scatter correction (AyCySy), and 5) filtered backprojection (FBP) with a Butterworth filter 0.034 mm^{-1} cut-off frequency and order 5.2. FBP was included to compare the results obtained with the iterative algorithms with those achieved with the standard reconstruction method.

D. Quantification

Quantitative results were obtained by calculating the contrast, defined as the striatal to background uptake ratio. The striatal uptake was calculated as the mean value in caudate or putamen. The background was obtained as the mean value in an occipital area. The contrast recovery (CR), defined as the ratio between the calculated and the theoretical contrast, was also used. The optimal value of this parameter is 1 in all cases, thereby facilitating comparison between results corresponding to different striatal to background uptake ratios.

III. RESULTS

Figure 2 shows the reconstructed images after 5 (top) and 30 (middle) iterations for 3.5 million counts, and after 30 iterations for 35 million counts (bottom). Images in each row correspond to AnCnSn, AyCnSn, AyCySn and AyCySy reconstructions. Figure 2 also shows the profiles along the horizontal line indicated in the top left image. The theoretical striatal/background ratio in this case was 7.

We can observe the improvement in the image quality when correction for degradations is consecutively incorporated in reconstruction. At 30 iterations, images are quite noisy, even when correction for collimator response is included. However, caudate and putamen are more clearly separated after 30 iterations than after 5 iterations, especially when collimator response is included in the reconstruction. These results are consistent with the fact that the higher the number of iterations, the greater the recovery of high spatial frequency components of the images. The plots enable us to appreciate the improvement in resolution when 30 iterations were performed and correction for all degradations was included in the reconstruction. A more marked minimum reflects the clearer separation between caudate and putamen. These results indicate that although 30 iterations should be regarded as too excesive for visual evaluation, can be considered as satisfactory in this case.

The effect of including compensation of degradations can be better observed on the bottom row, which corresponds to 35 million counts (after adding the 10 projection runs). The good quality of the image after 30 iterations and correction for all degradations should be pointed out.

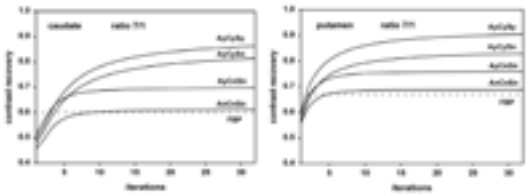

Figure 3. Contrast recovery parameter (CR) as a function of the number of iterations for caudate (left) and putamen (right). The plots correspond to CR values when reconstruction was performed without corrections (AnCnSn), with only attenuation correction (AyCnSn), with attenuation and collimator response correction (AyCySn) and with attenuation, collimator response and scatter correction (AyCySy). CR value obtained by using Filtered backprojection (FBP) appears as a horizontal dotted line for comparison.

To assess the improvement in reconstruction from a quantitative point of view, figure 3 shows CR as a function of the number of iterations for caudate and putamen. The plots correspond to the mean value of the ten runs. We can observe the improvement in quantification when correction of degradations was successively included in the transition matrix. We can also see that OSEM without corrections yields values that are comparable to those obtained with FBP. These results quantitatively support the idea that increasing iterations result in higher contrast.

Figure 4 shows the calculated versus the theoretical contrast for the different activity ratios simulated and when different corrections were performed (AyCySy, AyCySn, AyCnSn, AnCnSn and FBP). The identity line is also displayed to have a reference. In all cases, points can be fitted to a line with high correlation coefficients (r^2>0.95).

Table 1 shows the numerical values of CR obtained for striatal/background uptake ratios of 7/1, 5/1 and 3.5/1. Given the asympthotic behaviour of the plots in figure 3, we present the results after 30 iterations because the improvement after 30 iterations is almost negligible. The table also shows the importance of compensation of attenuation, collimator response and scatter to recover the true value of the striatal/background uptake ratio. In putamen, successive corrections of attenuation, collimator response and scatter shows an improvement of approximately 8 % on each step.

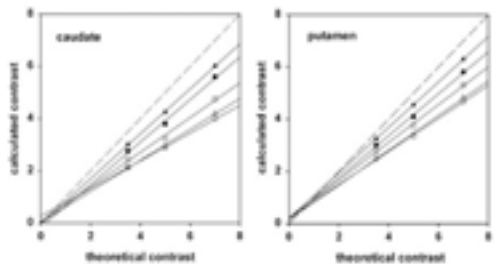

Figure 4. Calculated contrast versus theoretical contrast when corrections Are successively included in reconstruction: FBP (hollow circles). Hollow triangles (AnCnSn). Hollow squares (AyCnSn). Filled circles (AyCySn). Filled triangles (AyCySy). Regression lines (solid) and the identity straight line (dashed) are also plotted.

The improvement is 30 % if all corrections are taken together, thereby increasing CR from 0.69 to 0.90. The improvement is even higher for caudate. CR shows an average increase of 9 %, 16 % and 13 % when correction of attenuation, collimator response and scatter are successively incorporated in the reconstruction. In this case, the value of CR increases from 0.60 to 0.86, which represents an improvement of 43 %. The increase of 16 % in CR (double the value found for putamen) when the spatially variant fan-beam collimator response was incorporated in the transition matrix is worth noting. This can be explained by the smaller size of caudate with respect to putamen, which increases the importance of PSF in quantification.

Table 1. Contrast recovery values obtained after degradation corrections. The results correspond to striatal/background uptake ratios of 7/1, 5/1 and 3.5/1. Mean and standard deviations over ten runs are shown.

PUTAMEN

ratio	7/1	5/1	3.5/1
AyCySy	0.90 ± 0.02	0.91 ± 0.03	0.93 ± 0.04
AyCySn	0.83 ± 0.02	0.82 ± 0.04	0.86 ± 0.05
AyCnSn	0.76 ± 0.02	0.75 ± 0.04	0.80 ± 0.04
AnCnSn	0.69 ± 0.05	0.68 ± 0.04	0.72 ± 0.04
FBP	0.67 ± 0.02	0.67 ± 0.03	0.71 ± 0.03

CAUDATE

ratio	7/1	5/1	3.5/1
AyCySy	0.86 ± 0.03	0.85 ± 0.03	0.86 ± 0.03
AyCySn	0.80 ± 0.03	0.76 ± 0.04	0.79 ± 0.10
AyCnSn	0.68 ± 0.06	0.65 ± 0.02	0.70 ± 0.10
AnCnSn	0.60 ± 0.06	0.59 ± 0.02	0.61 ± 0.10
FBP	0.57 ± 0.02	0.58 ± 0.03	0.61 ± 0.05

IV. DISCUSSION

Our results highlight the importance of correcting degradations to improve quantification accuracy of neurotransmission SPET studies. In particular, spatially variant collimator/detector response plays a significant role in the quantification of small structures such as the basal ganglia.

In this study, we employed the ideal correction of scattered photons in an attempt to assess the influence of scattered photons on quantification. Thus, only primary photons from SimSET were considered when the effect of scatter correction was studied. Our findings confirm that scattering also plays an important role in striatal/background uptake quantification.

This study is valid for ^{99m}Tc ligand agents. However, if quantification is performed on ^{123}I agents SPET imaging, contamination of high-energy photons should be taken into account. Low-abundance (<3.5 %) high-energy photons emitted at 346, 440, 505 and 529 keV have a non-negligible contribution to projections due to septal penetration and inelastic scatter [21]. Thus, methods to compensate for this degradation should be used [21]. This study falls beyond the scope of this work, which is focused on improving resolution by introducing the spatial variant fan-beam collimator response in the transmission matrix. Further studies will be necessary to correct reconstructed images for this degradation.

In conclusion, our findings indicate that compensation for fan-beam collimator response results in a significant improvement of 8 % in putamen and 16 % in caudate in the recovery of the striatal/background ratio. This underlines the importance of improving resolution when small structures are involved in quantification. Improvement was 30 % in putamen and 43 % in caudate when correction of attenuation, spatially variant collimator response and scatter were included in the reconstruction. Thus, the values of normalized striatal/background ratio increased from 0.69 to 0.90 for putamen and from 0.60 to 0.86 for caudate after correcting all degradations. Our results suggest that the correction of these degradations can improve accuracy of quantification of neurotransmission SPET imaging.

V. REFERENCES

1. Tatsch K. Imaging of the dopaminergic system in parkinsonism with SPET. *Nucl Med Comm* 2001; 22:819-27.

2. Pilowsky LS. Probing targets for antipsychotic drug with PET and SPET receptor imaging. *Nucl Med Comm* 2001; 22:829-833.

3. Acton PD, Choi S-R, Plössl K, Kung HF. Quantification of dopamine transporters in the mouse brain using ultra-high resolution single-photon emission tomography. *Eur J Nucl Med* 2002; 29:691-698.

4. Tatsch K. Can SPET imaging of dopamine uptake sites replace PET imaging in Parkinson's disease?. *Eur J Nucl Med* 2002; DOI 10.1007/s00259-002-0814-5.

5. Frey KA. Can SPET imaging of dopamine uptake sites replace PET imaging in Parkinson's disease?. *Eur J Nucl Med* 2002; DOI 10.1007/s00259-002-0815-4.

6. Booij J, Tissingh G, Winogrodzka a, Van Royen EA. Imaging of the dopaminergic neurotransmission system using single-photon emission tomography and positron emission tomography in patients with parkinsonism. *Eur J Nucl Med* 1999; 26:171-82.

7. Neumeyer JL, Wang S, Milius RA et al. *N*-omega-fluoroalkyl analogs of (IR)-2 beta-carbomethoxy-3 beta-(4-iodophenyl)-tropane (beta-CIT): radiotracers for positron emission tomography and single photon emission computed tomography imaging of dopamine transporters. *J Med Chem* 1994; 37:558-561.

8. Kung MP, Stevenson DA, Plössl K, Meegalla SK, Beckwith A, Essman WD, Mu M, Lucki I, Kung HF. [^{99m}Tc]TRODAT-1: a novel technetium-99m complex as a dopamine transporter imaging agent. *Eur J Nucl Med* 1997; 24:372-80.

9. Johannsen B, Pietzsch HJ. Development of technetium-99m-based CNS receptor ligands: have there been any advances?. *Eur J Nucl Med* 2002; 29:263–75.

10. El Fakhri G, Moore SC, Maksud P, Aurengo A, Kijewski MF. Absolute Activity Quantitation in Simultaneous 123I/99mTc Brain SPECT. *J Nucl Med* 2001; 42:300–8.

11. Habraken JB, Booij J, Slomka P, Sokole EB, von Royen EA. Quantification and visualization of defects of the functional dopaminergic system using an automatic algorithm. *J Nucl Med* 1999; 40:1091-97.

12. Radau P, Linke R, Slomka PJ, Tatsch K. Optimization of automated quantification of ^{123}I-IBZM uptake in the striatum applied to parkinsonism. *J Nucl Med* 2000; 41:220-7.

13. Booij J, Tissingh G, Boer GJ, Speelman JD, Stoof JC, Janssen AGM, Wolters EC, Vanroyen EA [^{123}I]FP-CIT SPECT shows a pronounced decline of striatal dopamine transporter labelling in early and advanced Parkinson's disease. *J Neurol Neurosurg Psychiatry* 1997; 62:133-40.

14. Mozley PD, Schneider JS, Acton PD, Plossl K, Stern MB, Siderowf A, Leopold NA, Li PY, Alavi A, Kung HF. Binding of [^{99m}Tc]TRODAT-1 to dopamine transporters in patients with Parkinson's disease and in healthy volunteers. *J Nucl Med* 2000; 41:584-589.

15. Seibyl JP, Marek K, Sheff K, Baldwin RM, Zoghbi S, Zea-Ponce Y, Charney DS, van Dyck CH, Hoffer PB, Innis RB Test/retest reproducibility of iodine-123-β-CIT SPECT brain measurement of dopamine transporters in Parkinson's patients. *J Nucl Med* 1997; 38:1453-9.

16. Linke R, Gostomzyk J, Hahn K, Tatsch K. [I-123]IPT-binding to the presynaptic dopamine transporter: variation of intra- and interobserver data evaluation in parkinsonian patients and controls. *Eur J Nucl Med* 2000; 27:1809-12.

17. Stoof JC, Winogrodzka A, van Muiswinkel FL, Wolters EC, Voorn P, Groenewegen HJ, Booij J, Drukarch B. Leads for the development of neuroprotective treatment in Parkinson's disease and brain imaging methods for estimating treatment efficacy. *Eur J Pharmacol* 1999; 375:75-86.

18. Hudson HM and Larkin RS. Accelerated image reconstruction using ordered subsets projection data *IEEE Trans Med Imaging* 1994; 13:601-9

19. Harrison RL, Vannoy SD, Haynor SB, Gillispie SB, Kaplan MS, Lewellen TK. Preliminary experience with the photon history generator module of a public-domain simulation system for emission tomography. *IEEE NSS-MIC Conf. Record* 1993; 2:1154-8.

20. Buvat I, Rodriguez-Villafuerte M, Todd-Pokropek A, Benali H, Di Paola R. Comparative assessment of nine scatter correction methods based on spectral analysis using Monte Carlo simulations. *J Nucl Med* 1995; 36:1476-88.

21. El Fakhri G, Maksud P, Kijewski MF, Habert MO, Todd-Pokropek A, Aurengo A, Moore SC. Scatter and cross-talk corrections in simultaneous Tc-99m/I-123 brain SPECT using constrined factor analysis and artificial neural networks. *IEEE Trans Nucl Sci* 2000; 47:1573-80.

22. Pareto D, Pavia J, Falcon C, Juvells I, Ros D. Characterisation of fan-beam collimators. *Eur J Nucl Med* 2001; 28:144-9.

23. Cot A, Sempau J, Pareto D, Bullich S, Pavia J, Calviño F, D. Ros. Evaluation of the geometric, scatter and septal penetration components in fan beam collimators using Monte Carlo simulation *IEEE Trans Nucl Sci* 2002; 49:12-16.

24. Pareto D, Cot A, Falcon C, Juvells I, Pavia J, Ros D. Geometrical Response Modeling In Fan Beam Collimators. A Numerical Simulation. *IEEE Trans Nucl Sci* 2002; 49:17-24.

Assessment of SPM analysis in the comparison of two sets of ^{99m}Tc-HMPAO brain SPECT studies. A numerical simulation study.

D. Pareto[1,2], J. Pavía[2,3], A. Cot[4], C. Falcón[1,5], A. Benabarre[6], F. Lomeña[2,3], E. Vieta[3,6], D. Ros[1,3]

Abstract--**Statistical Parametric Mapping (SPM) has become the technique of choice to statistically evaluate PET, fMRI and SPECT functional brain studies. Nevertheless, only a few methodological studies have been carried out to assess the performance of SPM in SPECT. The aim of this work was to study the performance of SPM in detecting changes in regional cerebral blood flow (rCBF) in both hypo- and hyperfused situations. The paper seeks to determine the relationship between the group size and the rCBF changes, and the influence of the correction of attenuation, scatter and of variant collimator response on the group size. The assessment was carried out using simulated brain SPECT studies. Projections were obtained with Monte Carlo techniques and a fan-beam collimator was considered in the simulation process. Reconstruction was performed by using Ordered Subsets Expectation Maximization (OSEM) algorithm with and without compensation of attenuation, scattering and spatial variant collimator response.**

Our findings indicate that correction of degradations improves the calculation of the activation factor. The improvement was 12%, 10% and 3% on average in foci of 1.0, 2.1 and 3.7 cm^3. As regards SPM analysis, no changes in sensitivity were observed in the detection of hypo- and hyperperfused regions. Our results also show that correction of degradations diminishes the number of pairs in detecting changes in rCBF. For an activation factor of 15 % and a focus size of 1 cm^3 the number of pairs was 13 with correction and 17 without correction, whereas for a focus size of 3.7 cm^3 these values were 5 and 7, respectively. When the activation factor was 25 % the number of pairs was 8 and 11 for the focus of 1 cm^3, and 5 and 7 for the focus size of 3.7 cm^3.

Key Words: SPECT, SPM, OSEM, fan-beam, rCBF.

I. Introduction

Brain perfusion SPECT allows us to detect changes in regional cerebral blood flow (rCBF). This is of especial interest since rCBF has proved to be a sensitive parameter in the diagnosis of some neurological and psychiatric diseases and in identifying the cerebral regions involved in cognitive tasks. In these studies, statistical inferences have classically been made from mean values and standard deviations of the activity in predefined regions of interest (ROIs) in a group of subjects. In the last years, new tools have been developed to objectively evaluate statistical significance without previous selection of the involved brain regions. Thus, Statistical Parametric Mapping (SPM) has become, since its appearance in 1991, the technique of choice to statistically evaluate PET, fMRI and SPECT functional brain studies [1].

SPM employs a robust statistical analysis with a strong theoretical basis. Nevertheless, methodological works are necessary to assess the performance of the method in the different functional imaging techniques and, in particular, in SPECT. Accurate studies [2-4] have been performed to validate the SPM technique in activation SPECT studies. These authors simulated specific situations in which the activity distribution of the source was known and all parameters were controlled.

Assessment of SPM in SPECT has mainly been carried out on neuroactivation tasks, in which rCBF shows an increase. Nevertheless, neurological and psychiatric diseases such as atrophy, degeneration, and functional impairment are related to hypoperfusion in specific regions rather than to hyperperfusion [5]. SPM can also play a major role in identifying such specific regions or in assessing the response to a pharmacological treatment.

The aim of this work was to extend the study of SPM to situations in which rCBF can either increase or decrease. The paper seeks to determine the relationship between the group size and the rCBF changes, and the influence of the correction of attenuation, scatter and of variant collimator response on the group size. The study was carried out using numerical simulation. Fan-beam collimators, which are commonly employed in brain SPECT because of the good trade-off between resolution and noise, were considered. Realistic simulation of projections was obtained by using Monte Carlo techniques of transport of radiation. Reconstruction employed Ordered Subsets Expectation Maximization (OSEM) algorithm. Reconstruction was performed with and without compensation of attenuation, variant collimator response and scattering.

This work was supported in part by CICYT (SAF99/0137, SAF2002-04270-C02-02, FIS-PI020485). D. Pareto is funded by Universitat Barcelona (UB).
[1]Unitat Biofísica, Facultat de Medicina. UB (Spain).
[2]Servei de Medicina Nuclear, Hospital Clínic, Barcelona (Spain).
[3]Institut d'Investigacions Biomèdiques August Pi i Sunyer (IDIBAPS).
[4]Dept de Física i Enginyeria Nuclear, Universitat Politècnica de Catalunya.
[5]Serveis Científico Tècnics, UB.
[6]Institut de Psiquiatria i Psicologia, Hospital Clínic.
Correspondence to: D.Ros domenec@medicina.ub.es.

II. MATERIALS AND METHODS

Numerical simulation was employed to assess the performance of SPM in detecting changes in rCBF. The main characteristics of this process are described below: 1) the numerical brain phantom used, 2) how the projections were simulated, 3) the reconstruction algorithm , 4) how rCBF changes were quantified and 5) the statistical analysis employed.

Brain phantom

The digitized Zubal human brain phantom [6] was used to model the blood flow pattern. The matrix size of this numerical phantom was 256x256x120, with voxel size 1.04x1.04x1.40 mm^3. Values of 100, 25 and 4 were assigned to grey matter, white matter and cerebral spinal fluid in order to simulate the relative concentrations observed in the blood flow pattern [5].

Figure 1. Transaxial sections of the Zubal phantom (left) and its corresponding activity distribution (center) and attenuation map (right).

The non-uniform attenuation map was obtained by assigning 0.014 mm^{-1} to the linear attenuation coefficient of the brain tissue structures, and 0.030 mm^{-1} to bone. Figure 1 shows one central transaxial section of the Zubal phantom and its corresponding activity distribution and attenuation map.

Foci of different sizes were placed in the corpus cingulus, a brain area involved in neuroactivation as well as in mood disorders [7-9]. Non-spherical foci were obtained by positioning spheres of 15, 20 and 25 mm in diameter in the corpus cingulus and intersecting them with the gray matter. The final volumes of the three foci were 1.0, 2.1 and 3.7 cm^3. Figure 2 shows one transaxial section and one saggital section corresponding to the foci of 3.7 cm^3. Note the non-spherical shape of the foci.

Values of –75, -50, -25, -20, -15, +15, +20, +25, +50 and +75 were assigned to the foci, thus mimicking hypo- or hyperfused regions. Given that the basal value of the gray matter was 100, these values also represented the percentage of change in rCBF. These regions will be referred to as activated regions despite increases or decreases in rCBF.

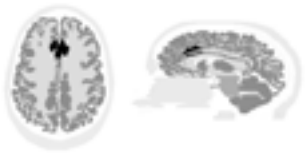

Figure 2. Transaxial (left) and saggital (right) views of the Zubal phantom showing the foci in the corpus cingulus.

Projections

The SimSET Monte Carlo [10] code was employed to obtain SPECT projections of the activity distribution. SimSET generates realistic sets of projections by including all the physical effects that the photons undergo in its interaction with the matter during the acquisition process. The simulation conditions were:

a. The photon history generator module included the tracking of 942 million photons in order to obtain projections with approximately 12 million detected photons. The energy of the photons generated was 140 keV, corresponding to the emission of ^{99m}Te.

b. The binning module included 60 projections over 360° of 128x128 pixels each, with a pixel size 4.4x4.4 mm^2. An energy window selected photons ranging from 126 to 156 keV. Primary and scattered photons were collected in separate files, thereby allowing for simulation of the ideal scatter correction.

c. The collimator module incorporated a converging fan-beam cast collimator with focal distance F=355 mm, hole side w=0.866 mm, septal thickness t_s=0.2 mm, length L=40 mm, distance from the back collimator plane to the detector plane B=8mm and field of view (FOV) of 530x250 mm. These parameters correspond to a high resolution cast fan beam collimator (Van Mullekom, Holland) of a Helix HR double-headed gammacamera (Elscint, Haifa).

d. The detector module incorporated a NaI scintillator crystal. The intrinsic energy resolution function of this detector was modeled as a Gaussian distribution with FWHM of 11% for 140keV. The rotation radius was fixed at 140 mm.

Two groups were simulated to mimic the conditions for a statistical comparison. The first one corresponded to the basal studies or control group. The second group corresponded to the studies with changes in rCBF in the corpus cingulus. Twenty SimSET simulations with different random seeds were carried out in the first group. Given the number of factors (10), foci sizes (3) and runs (20), we followed a different strategy, in the second group, in order to diminish the number of simulations to obtain the 600 data set projections needed. We took advantage of the fact that SimSET simulation is intrinsically additive and, as a consequence, the projections of the "activated" Zubal phantom could be obtained by adding the projections of the original phantom and those corresponding to the foci. Thus, first we performed 20 new simulations representing real noise of the original Zubal phantom. Then, the simulation of the 3 foci was carried out separately, but in these cases the number of photons tracked was high enough to ensure that these projections had no-significant noise. To this end, 74, 147 and 260 million histories were tracked, respectively. With this number of photon histories the signal-to-noise ratio defined as the ratio between the sum of weights and the sum of square weights was greater than10^3, thus indicating that the noise in the projections could be ignored. Generating projections of foci with such a low noise level allowed us to obtain the different levels of activation from –75 to +75 by multiplying the original projections of the foci by the corresponding factor. This strategy enabled us to diminish the number of

simulations from 600 to 23.

Computer time to simulate projections of the original Zubal phantom with 12 Mc was about 4 hours on PC workstation with a double processor AMD-K7 mp 1.44 GHz.

Reconstruction

Projections were reconstructed by using Ordered Subsets Expectation Maximisation (OSEM) [11], with 10 subsets and 8 iterations. Reconstruction was performed with (C) and without (NC) correction of attenuation, collimator/detector response and scatter in order to assess the significance of corrections in SPM analysis.

Attenuation correction was performed in the reconstruction process by including the non-uniform attenuation map in the projector/backprojector pair. Compensation of fan-beam collimator response was carried out by incorporating the spatially variant point spread function (PSF) into the transition matrix [12]. Ideal correction of scattering was performed by using only primary photons in the reconstruction process.

The reconstruction parameters were 64x64 matrix size and 4.16 mm pixel size.

Quantification

Activation factors were calculated in order to assess the goodness of the reconstruction and the significance of correction of degradations. The activation factor (AF) was obtained as AF=100·(A-B)/B, where A and B represent the mean values of the activated and basal images in a ROI placed on the three activated foci. In order to minimize border effects, the volume of this ROI was 0.4 cm^3. This ROI was obtained by locating a sphere of 10 mm in diameter in the corpus cingulus and intersecting it with the gray matter.

Statistical methods

To statistically evaluate the differences between the basal and activated studies, Statistical Parametric Maps of rCBF were obtained with SPM99 (Matlab 6.0 on a Linux PC workstation). Both basal and activated images were normalized to the SPECT template space using a 9-parameter transformation. Normalized images, with 3x3x3mm^3 voxel size, were smoothed with a three dimensional Gaussian filter of 10 mm full-width-at-half-maximum (FWHM). Proportional scaling was employed to remove global changes with a threshold masking of 0.8 in the statistical analysis [13].

Differences were evaluated with a Compare-population (1scan/subject) design and significant differences were evaluated simultaneously at a cluster and voxel level, $p<0.05$ corrected.

III. RESULTS

Figure 3 shows the calculated versus the theoretical activation factor for the three volumes of the activated areas. The factors were obtained by using OSEM with (circles) and without (triangles) correction of degradations. The results correspond to mean values on the 20 runs. It can be observed that in the three graphs the circles are closer than triangles to the identity line, which indicates that the correction of degradations improves the calculation of the activation factor. To quantitatively evaluate this improvement, a recovery activation factor (RAF) was employed. RAF was defined as $RAF=AF/AF_t$, where AF_t represents the theoretical activation factor. RAF increased 12% on average in foci of 1.0 cm^3 (from 66 % without correction to 78 % with correction), 10 % in foci of 2.1 cm^3 (from 83% to 93%), and 3% in foci of 3.7 cm^3 (from 90% to 93%). The relative errors were 2% on average for both reconstruction strategies. These errors determine the sensitivity in the detection of the activated factors using 20 basal/activated pairs.

This improvement should mainly be attributed to the PSF correction although the fact that RAF does not attain 100% indicates that the resolution recovery is not complete when the correction for the spatially variant PSF is carried out. Nevertheless, the recovery is as high as 93% for foci sizes of 2.1 and 3.7 cm^3

Table 1 shows the number of pairs needed to detect the simulated foci. Qualitatively, the results exhibit the expected behavior, i.e. the number of pairs increases when the activation factor decreases, and the group size decreases as the focus volume increases. From a quantitative point of view, the results of table 1 show that correction of

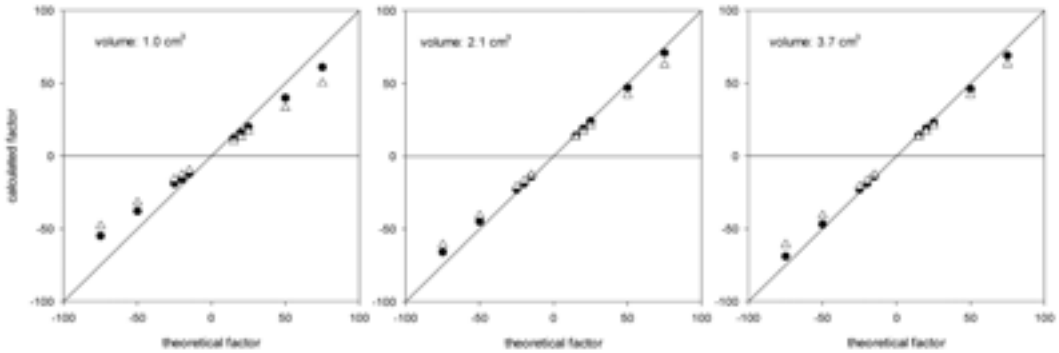

Figure 3. Calculated versus theoretical activation factor obtained from images reconstructed by using OSEM with (circles) and without (hollow triangles) correction of degradations and for volumes of the activated region of 1.0 cm^3, 2.1 cm^3, and 3.7 cm^3. The identity line is also plotted to facilitate comparison.

degradations could play a role when a slight hypo- or hyperperfusion occurs in small foci.

Table 1. Number of pairs needed to detect the foci of 1.0, 2.1 and 3.7 cm^3 with (C) and without (NC) correction of degradations as a function of the activation factor.

Activation	1 cm^3		2.1 cm^3		3.7 cm^3	
factor (%)	C	NC	C	NC	C	NC
-75	5	5	4	5	4	4
-50	5	6	4	5	4	4
-25	8	11	5	6	5	6
-20	9	14	5	7	5	6
-15	13	17	5	12	5	7
15	13	18	5	13	5	7
20	9	14	5	7	5	6
25	8	11	5	6	5	6
50	5	6	4	5	4	4
75	4	6	4	5	4	4

The results of table 1 correspond to the maximum number of pairs obtained after repeating statistics using random selections of the studies. However, on some occasions the number of pairs was lower than those indicated in table 1. Such a restrictive criterion was imposed to maintain the sensitivity and the specificity of the voxel-based statistical analysis within acceptable limits when SPM is employed in real SPECT studies.

Table 1 does not show differences between the number of pairs in detecting hypo- and hyperfusion, thereby suggesting that the sensitivity of SPM does not depend on the whether the rCBF change is positive or negative.

Theoretical arguments indicate that the behavior of the relationship between the group size and the activation factor should be asymptotic in both directions. Hence, an inverse function was fitted to the data in table 1 [3]:

$$NP = a + \frac{b}{F - c}$$

Where F is the activation factor and NP is the number of pairs needed to detect this change.

Figure 4 shows the values of table 1 and the fitted inverse functions. The fittings obtained by using this empirical model showed correlation coefficient values ranging between 0.80 and 0.99. It can be seen in figure 4 that correction of degradations could be significant for activation factors lower than 20 %. The plots in Figure 4 qualitatively highlight the usefulness of the correction of degradations. Nevertheless, the quantitative utility of these curves is restricted to values of F in the interval [15%, 25%] given that ours results were obtained from the values of F in this interval. Outside the interval, the number of pairs necessary for detection can be estimated from the inverse function, but the extrapolation may be wrong for values removed from [15%, 25%]. Thus, further studies will be necessary to determine the group size and the significance of correction of degradations when the activation factors are lower than 15 %.

In summary, our findings suggest that SPM has the same sensitivity in detecting both hypo- as hyperperfused regions, and that correction of degradations diminishes the number of pairs in the detection of changes in rCBF. Moreover, some other reasons also point to the usefulness of correcting for degradations. This is a preliminary study to test the methodological approach with the result that the assessment of SPM was done in a simple and well-controlled situation. This enabled us to determine the limit of sensitivity of SPM, i.e. the minimum group size in an ideal situation. For this reason, physiological and anatomical variability of the brain was not simulated and, as a consequence, the influence of this potential effect in SPM analysis was not considered in this work. In a real context, this variability would result in an increase in the variance of data if degradations were not corrected, e.g. changes in brain size and in rotation radius yield changes in the pixel values of the reconstructed images. Brain size affects the significance of attenuation and scatter in projections. Rotation radius has an influence on resolution given that the PSF depends on the distance between the point source and the collimator. For these reasons, pixels of the same activity placed in equivalent regions in brains of varying size will yield disparate values in images reconstructed without correction of degradations. This leads to a non-real increase in the variance of data, which results in a loss of sensitivity of SPM. By contrast, correction of degradations yields reconstructed images that are more similar to one another and more suitable for the standardization process inherent in SPM analysis.

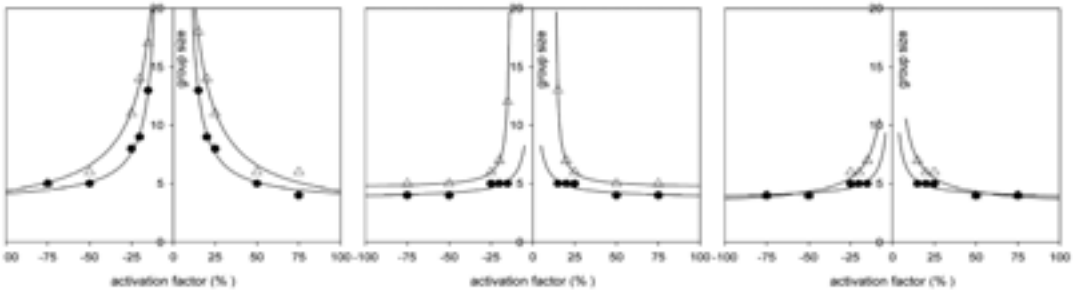

Figure 4. Number of studies needed to detect the foci as a function of the activation factor. These results were obtained from images reconstructed by using OSEM with (circles) and without (hollow triangles) correction of degradations and for volumes of the activated region of 1.0 cm^3 (left), 2.1 cm^3 (middle), and 3.7 cm^3 (right). The fitted inverse function (in solid line) is also plotted.

IV. CONCLUSIONS

Monte Carlo simulation was employed to numerically obtain projections in ^{99m}Tc brain SPECT studies. The use of a Monte Carlo projector different from the projector/reprojector pair employed in reconstruction eliminates bias, thus ensuring reliable results.

Our findings indicate that correction of degradations improves the calculation of the activation factor. The improvement was 12%, 10% and 3% on average in foci of 1.0, 2.1 and 3.7 cm^3. Thus, when correction of degradations was included in the reconstruction algorithm, the calculated activation factor attains 78%, 93% and 93 % of the theoretical activation factor for the foci of 1.0, 2.1 and 3.7 cm^3.

As regards to SPM analysis, no changes in sensitivity were observed in the detection of hypo- and hyperperfused regions. Our results also show that correction of degradations diminishes the number of pairs in detecting changes in rCBF. This diminution is more important for low values of the activation factor and for small focus size. Thus, for an activation factor of 15 % and a focus size of 1 cm^3 the number of pairs is 13 with correction and 17 without correction, whereas for a focus size of 3.7 cm^3 these values were 5 and 7, respectively. When the activation factor was 25 % the number of pairs was 8 and 11 for the focus of 1 cm^3, and 5 and 7 for the focus size of 3.7 cm^3.

V. REFERENCES

1. http://www.fil.ion.ucl.ac.uk/spm
2. Lahorte P, Vandenberghe S, Van Laere K, Audenaert K, Lemahieu I, Dierckx RA (2000) "Assessing the performance of SPM analyses of spect neuroactivation studies"; *Neuroimage* 12 757.
3. Van Laere K , Versijpt J, Koole M, Vandenberghe S, Lahorte P, Lemahieu I, Dierckx (2002) "Experimental performance assessment of SPM for SPECT neuroactivation studies using a subresolution sandwich phantom design"; *Neuroimage* 16 200.
4. Stamatakis EA, Wilson JTL, Wyper DJ (2001) "Spatial normalization of lesioned HMPAO-SPECT images" *Neuroimage* 14 844.
5. Catafau AM (2001) "Brain SPECT in clinical practice. Part I: perfusion"; *J Nucl Med* 42 259.
6. Zubal I, Harrel CR, Smith ED, Rattner Z, Gindi G, Hoffer PB (1994) "Computing three-dimensional segmented human anatomy"; *Med Phys* 212 299.
7. Ito H, Kawashima R, Awata S, Ono S, Sato K, Goto R, Koyama M, Sato M, Fukuda H (1996) "Hypoperfusion in the limbic system and prefrontal cortex in depression: SPECT with anatomic standardization technique"; *J Nucl Med* 37 410.
8. Migneco O, Benoit M, Koulibaly PM, Dygai I, Bertogliati C, Desvignes P, Robert P, Malandain G, Bussiere F, Darcourt J (2001) "Perfusion brain SPECT and Statistical Parametric Mapping indicate that apathy is a cingulate syndrome: a study in Alzheimer's disease and nondemented patients"; *Neuroimage* 13 896.
9. Peoples LL (2002) "Will, anterior cingulate cortex and addiction"; *Science* 296 1623.
10. Harrisson RL, Haynor DR, Gillispie SB, Vannoy SD, Kaplan MS, Lewellen TK (1993) "A public-domain simulation system for emission tomography. Photon tracking through heterogeneous attenuation using importance sampling" *J Nuc Med* 34 60.
11. Hudson HM, Larkin RS (1994) "Accelerated image-reconstruction using ordered subsets of projection data" *IEEE Trans Med Imag* 13 601.
12. Pareto D, Pavía J, Falcón C, Juvells I, Cot A, Ros D (2000) "Characterisation of fan-beam collimators"; *Eur J Nuc Med* 28 144-149.
13. Acton PD, Friston KJ (1998) "Statistical parametric mapping in functional neuroimaging: beyond PET and fMRI activation studies"; *Eur J Nuc Med* 25 663.